Experimental and numerical investigation of two physical mechanisms influencing the cloud cavitation shedding dynamics

Petar Tomov, Kilian Croci, Sofiane Khelladi, Florent Ravelet, Amélie Danlos, Farid Bakir, Christophe Sarraf

Experimental and numerical investigation of two physical mechanisms influencing the cloud cavitation shedding dynamics

Petar Tomov,[1, a)] Kilian Croci,[1] Sofiane Khelladi,[1] Florent Ravelet,[1, b)] Amélie Danlos,[2] Farid Bakir,[1] and Christophe Sarraf[1]

[1)] *DynFluid Laboratory, Arts et Métiers ParisTech, 151 Boulevard de l'Hôpital, Paris 75013, France*

[2)] *Laboratoire du Génie des Procédés pour l'Energie, l'Environnement et la Santé, Conservatoire National des Arts et Métiers, 292 rue Saint Martin, 75003 Paris, France*

(Dated: submitted 5 March 2016)

The paper presents numerical and experimental investigations of the existence of two different physical mechanisms as principal origin of cloud cavitation shedding. The two mechanisms are the re-entrant jet formed at the cavity closure region and the shock wave propagation due to the condensation of vapor structures. The experimental observations of these phenomena are done at a fixed Reynolds number of about 1.2×10^5 by means of a high-speed camera on a transparent horizontal Venturi nozzle with $18°/8°$ convergent/divergent angles, respectively. A wavelet analysis is applied with several cavitation numbers in order to associate some image series to the occurrence frequencies of the two shedding mechanisms. In complement, a numerical model is performed in order to access to a 3D representation of the different phenomena. The compressible Navier-Stokes equations coupled with the Homogeneous Equilibrium Mixture Model are solved with a Finite Volume solver based on Moving Least Squares approximations. A snapshot Proper Orthogonal Decomposition technique is applied on both numerical and experimental results. The energy levels of different modes from numerical and experimental data are found to be in a good agreement. Instantaneous pressure peaks of the order of 10 bar, associated with erosive condensation shock wave, are numerically identified. The 3D numerical simulations reveal also that side-entrant jet flow is partially responsible for the re-entrant jet influence on the cloud cavitation shedding.

Keywords: Cavitation Shedding, Re-entrant Jet, Condensation Shock Wave, Numerical Simulations, HEM, POD, Wavelet, Venturi

I. INTRODUCTION

Cavitation is the vapor formation inside a liquid due to a pressure drop. This phenomenon is observed in various technical applications in different engineering fields. The cavitation is responsible for issues like erosion[1], noise and vibrations[2] which can lead to a malfunctioning of various turbo-machines[3], for instance impellers[4]. The cavitation occurrence has a negative effect on the proper functioning of a hydraulic system and different cavitation controlled systems[5,6] can be implemented to reduce these negative aspects. However, there are some cases where it can have an extremely positive effect such as drag reduction of submarine vehicles[7]. Indeed, the supercavitating structure covers the immersed body and makes it slip through the liquid[8], which results in a extremely rapidly moving object but with some instabilities. Therefore, it is of crucial importance for one to understand the physics behind the multiphase flow, in order to reduce the negative effect or increase its positive one.

Unsteady cloud cavitation shedding has been widely studied experimentally during past decades for different geometries such as hydrofoil profiles[9–11], spheres[6] or Venturi nozzles[5,12,13]. These studies tend to show that this unsteadiness is due to a frothy re-entrant jet reaching back the cavity. For small cavities, this re-entrant jet thickness is in the order of the cavity thickness and an adverse pressure peak tends to stabilize the cavity closure. It results in a closed cavity where the re-entrant jet generates a stable vapor/liquid mixed cavity. For bigger cavities, the adverse pressure gradient at cavity closure is decreased enough in order that the re-entrant jet reaches the top of the cavity and, as a result, cuts the vapor phase in two, the downstream partial cavity being next advected by the flow. Pham et *al.*[10] find a correspondence between the re-entrant jet and the cloud shedding occurrence. As a result, the repeatability of the process can be characterized by the shedding cycle[9,11] and a frequency f_s. Recently Ganesh et *al.*[14] proved experimentally with X-ray measurements that the shedding mechanism may not be governed only by the re-entrant jet, but also by the propagation of vapor-shock waves in the bubbly mixture which occurs at a frequency f_w. These two shedding mechanisms can be influenced by some features such as scale effects and aspect-ratio investigated by Dular et *al.*[13] which can have multiple influences on the cavity dynamic (as the creation of a side-entrant jet for small but wide Venturi nozzles).

The data acquired in these studies permits to access to valuable 2D outcomes of the cavity dynamic (cavity length, shedding frequencies) for a large array of pressure

[a)] Electronic mail: petar.tomov@ensam.eu
[b)] Electronic mail: florent.ravelet@ensta.org

and velocity conditions. However numerical simulations (particularly in 3D) are necessary to validate the different mechanisms described before and to capture some cavity dynamics hardly perceptible with experimental observations. In this context, Decaix et *al.*[15] studied numerically the behavior of cloud cavitation developing along a Venturi type nozzle by a compressible one-fluid model. In the same manner Chen et *al.*[16] did a numerical and experimental study of unsteady sheet and cloud cavitation flows in a convergent-divergent nozzle. Dittakavi et *al.*[17] and Charriere et *al.*[18] separately studied the turbulence interaction and different turbulence models in a series of large eddy simulations in a Venturi nozzles. It has been proven that the major source of vorticity is the collapse of the vapor structures which also results in the formation of hair-pin vortex structures. All of the studies show different aspects of a periodic cycling which can take place in the case of a Venturi nozzle.

The purpose of the present study is multifold. Firstly, the double Venturi nozzle geometry allows the observation and exploration about the symmetry of the sheet cavities at the top and bottom walls, as well as their coupling under the influence aspect ratio and of the interaction between the advected structures. Secondly, the paper puts forward experimental and numerical evidences of the presence of the re-entrant jet, side-entrant jet and condensed shock waves in the cloud cavitation shedding regime.

The article is organized into four major sections. Section II presents both the experimental setup and the numerical modeling. Section III deals with the results and discussions. The article ends by concluding remarks given in Sec. IV.

II. EXPERIMENTAL SETUP AND NUMERICAL MODELING

A. Experimental setup

The experiments were conducted in a hydrodynamic loop of the DynFluid Laboratory fully described in a previous work of Tomov et *al.*[19]. As a reminder, the loop consists of two tanks of 150 L capacity each connected by cylindrical pipe with inner diameter of 40 mm. Between the two tanks is placed the test section, represented in Fig. 1, consisting in two transparent horizontally symmetrical Venturi profiles with converging/diverging angles of 18° and 8°, respectively.

The throat height is $H_{throat} = 10$ mm and the width is constant all along the test section and is equal to 10 mm.

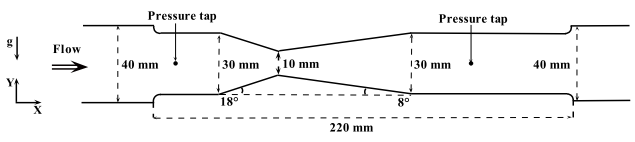

FIG. 1. Venturi nozzle geometry at scale

In the present study, lengths are expressed with non-dimensional values $X^\star = \frac{x}{H_{throat}}$ whereas the Reynolds is defined at the Venturi throat with H_{throat} and the reference velocity $V_{ref} = 12$ m.s^{-1} corresponding to the mean velocity at the throat section, since it is the place where the flow regime changes its nature. The experimental cavitation number is defined as $\sigma = \frac{(P_{ref} - P_{vap})}{\frac{1}{2}\rho V_{ref}^2}$ where P_{ref} is measured at $X^\star = -6$ from the inlet of the Venturi section. The value of σ is corrected removing 3% in order to take into account the real pressure at the throat. One can refers to the precedent study of Tomov et *al.*[19] for further information about the experimental set-up characteristics and the uncertainties of measurements. It is difficult to perfectly match the experimental and numerical values of the cavitation number. As a result, the pressure at the outlet section of the Venturi nozzle P_{out} is also expressed for numerical simulations such as the work of Schnerr et *al.*[20].

Clearly visible peaks in a frequency spectrum are generally related to spatial structures, which dispose with some characteristic dimension. The issue of universal definition of a Strouhal number in cavitation is not straightforward. It has been addressed, discussed and a proposal for its unification has been given by Dular et *al.*[21]. In the present paper, the choice is made to define the Strouhal number as $S_t = \frac{f H_{throat}}{V_{ref}}$ with f corresponding to a frequency of occurrence of a shedding feature.

B. Numerical modeling

1. Physical Model

The cavitating flows involve a very large variety of physical phenomena with different spatial and temporal scales. Typical examples are bubble or cloud vapor dynamics and non-equilibrium thermodynamics. As a result, it is difficult to fully resolve all scales, nevertheless the current state of the art of the computers. Therefore, the modeling of each phase (liquid, vapor or mixture) present in the multiphase cavitating flow is of crucial importance for the good representation of the physics of the flow.

The compressible Navier - Stokes equations written in cartesian coordinates without a source terms are given in their conservative form in Eq. 1.

$$\frac{\partial \mathbf{U}}{\partial t} + \frac{\partial}{\partial x}\left(\mathbf{F}_x(\mathbf{U}) - \mathbf{F}_x^V(\mathbf{U})\right) + \frac{\partial}{\partial y}\left(\mathbf{F}_y(\mathbf{U}) - \mathbf{F}_y^V(\mathbf{U})\right) + \frac{\partial}{\partial z}\left(\mathbf{F}_z(\mathbf{U}) - \mathbf{F}_z^V(\mathbf{U})\right) = \mathbf{0} \tag{1}$$

$$\mathbf{U} = (\rho \quad \rho u \quad \rho v \quad \rho w \quad \rho E)^T \tag{2}$$

$$\begin{cases} \mathbf{F_x}(\mathbf{U}) = \left(\rho u \quad (\rho u^2 + p) \quad \rho uv \quad \rho uw \quad (\rho E + p)u\right)^T \\ \mathbf{F_y}(\mathbf{U}) = \left(\rho u \quad \rho uv \quad (\rho v^2 + p) \quad \rho vw \quad (\rho E + p)v\right)^T \\ \mathbf{F_z}(\mathbf{U}) = \left(\rho u \quad \rho uv \quad \rho vw \quad (\rho w^2 + p) \quad (\rho E + p)w\right)^T \end{cases} \tag{3}$$

$$\begin{cases} \mathbf{F}_x^V(\mathbf{U}) = (\tau_{xx} \quad \tau_{xy} \quad \tau_{xz} \quad (u\tau_{xx} + v\tau_{xy} + w\tau_{xz} - q_x))^T \\ \mathbf{F}_y^V(\mathbf{U}) = (\tau_{yx} \quad \tau_{yy} \quad \tau_{yz} \quad (u\tau_{yx} + v\tau_{yy} + w\tau_{yz} - q_y))^T \\ \mathbf{F}_z^V(\mathbf{U}) = (\tau_{zx} \quad \tau_{zy} \quad \tau_{zz} \quad (u\tau_{zx} + v\tau_{zy} + w\tau_{zz} - q_z))^T \end{cases} \tag{4}$$

$$\begin{cases} \tau_{xx} = 2\mu\dfrac{\partial u}{\partial x} - \dfrac{2}{3}\left(\dfrac{\partial u}{\partial x} + \dfrac{\partial v}{\partial y}\right), \quad \tau_{yy} = 2\mu\dfrac{\partial v}{\partial x} - \dfrac{2}{3}\left(\dfrac{\partial u}{\partial x} + \dfrac{\partial v}{\partial y}\right), \\ \tau_{zz} = 2\mu\dfrac{\partial w}{\partial z} - \dfrac{2}{3}\left(\dfrac{\partial u}{\partial x} + \dfrac{\partial v}{\partial y}\right), \quad \tau_{xy} = \mu\left(\dfrac{\partial u}{\partial x} + \dfrac{\partial v}{\partial y}\right), \\ \tau_{xz} = \mu\left(\dfrac{\partial u}{\partial z} + \dfrac{\partial w}{\partial x}\right), \quad \tau_{yz} = \mu\left(\dfrac{\partial v}{\partial z} + \dfrac{\partial w}{\partial y}\right), \end{cases} \tag{5}$$

The conservative variables are expressed in Eq. 2 and the inviscid fluxes $\mathbf{F_x}(\mathbf{U})$, $\mathbf{F_y}(\mathbf{U})$, $\mathbf{F_z}(\mathbf{U})$ are given in Eq. 3. The viscous fluxes $\mathbf{F}_x^V$, $\mathbf{F}_y^V$, $\mathbf{F}_z^V$ are expressed in Eq. 4. In the above written equations, ρ stands for density, p for pressure and u, v, w are the velocity components. The viscous stresses are expressed in Eq. 5, where μ is the viscosity.

The heat fluxes are represented by Fourier's law:

$$q_x = -\lambda\frac{\partial T}{\partial x}, \quad q_y = -\lambda\frac{\partial T}{\partial y}, \quad q_z = -\lambda\frac{\partial T}{\partial z} \tag{6}$$

where T is denoted temperature and λ is the thermal conductivity.

The compressible Navier–Stokes equations are coupled with the Homogeneous Equilibrium Model (HEM) which was initially presented by Saurel et *al.*[22] The HEM model accounts for the mass, momentum, as well as the energy equations in the case of the homogeneous mixture flow. In the zones of cavitation, the conservation equations lose locally their hyperbolic nature and become elliptic. In order to deal with this issue, equations of state describe each phase separately. As a result, two phases keep their own thermodynamic properties[23]. The use of this model supposes the existence of a local thermodynamic equilibrium, therefore the liquid and vapor phase pressures are considered equal to the saturation vapor pressure, $p_v = p_l = p_{sat}(T)$, as well as the temperature of the two phases in the mixture, $T_v = T_l = T$. The model does not take into account any relative motion between phases. The void fraction ratio (α) calculation is based on the values of the saturation densities for the liquid and vapor phases. The void fraction ratio is first defined, followed by the equations of mixture density and mass conservation.

$$\alpha = \frac{\rho - \rho_{l.sat(T)}}{\rho_{v.sat(T)} - \rho_{l.sat(T)}} \tag{7}$$

The mixture density $\rho = \sum \rho_k \alpha_k$ is solution of Eq. 1, k being the phase indicator. From a numerical point of view, the major difficulty in cavitating flows lies in the proper treatment of two very different regions. The first one is the low-density pure vapor phase and the second one is high density the nearly incompressible liquid. Moreover, a special care must be taken for the transition mixture region, which is not always clearly distinguished. As a result, each of the liquid and vapor pure phases are described by a proper set of Equations of States (EoS). The fluid saturation properties are taken from Schmidt et *al.*[24].

2. Conservation system closure - Phases EoS

EoS liquid phase

The liquid phase is firstly described with EoS. The pressure of the liquid phase is governed by the modified Tait equation of state, where K_0 and N are constants[22]. The formulation considers the liquid phase as a saturated component of the multiphase flow.

$$p = K_0 \left[\left(\frac{\rho}{\rho_{l,sat}(T)} \right)^N - 1 \right] + P_{sat}(T) \tag{8}$$

Where $K_0 = 3.3 \times 10^8$ Pa and $N = 7.15$ for water. The temperature relation can be expressed in terms of the specific energy $T = \frac{e - e_{l0}}{C_{vl}} + T_0$, e being internal energy, $e_{l0} = 617$ J.kg^{-1} is internal energy at reference temperature $T_0 = 273.15$ K and $C_{vl} = 4180$ J.kg^{-1}.K^{-1} is the liquid specific heat at constant volume. Vogel–Fulcher–Tammann's law[25–27] gives the dynamic viscosity formulation:

$$\mu_l = A \times 10^{B/(T-C)} \tag{9}$$

In the case of water $A = 2.414 \times 10^{-5}$ Pa.s, $B = 247.8$ K and $C = 140.0$ K. Thermal conductivity of water is considered constant and it is taken $\lambda_l = 0.6$ W.m^{-1}.K^{-1}.

The formulation of the speed of sound is derived from the hypothesis that the acoustic pressure fluctuations can be neglected in comparison with the cavitation pressure. Equation 10 gives the speed of sound in pure liquid. More information about its derivation is given in Appendix A.

$$c_l^2 = \frac{N(p - p_{sat}(T) + K_0)}{\rho} + \frac{p}{\rho^2 C_{vl}} \left(\frac{\partial p_{sat}(T)}{\partial T} - \frac{N(p - p_{sat}(T) + K_0)}{\rho_{l,sat}(T)} \frac{\partial \rho_{sat}(T)}{\partial T} \right) \tag{10}$$

EoS vapor phase

The EoS for the vapor phase are described below. The main hypothesis behind the vapor phase is its consideration as a perfect gas, hence the following relation is applied:

$$p = (\gamma - 1)\, \rho e \tag{11}$$

The temperature equation is written in terms of the latent heat of vaporization $L_v(T_0) = 2.753 \times 10^6$ J.kg^{-1} at temperature $T_0 = 273.15$ K as $T = \frac{e - e_{l0} - L_v(T_0)}{C_{vv}} + T_0$, $C_{vv} = 1410.8$ J.kg^{-1}.K^{-1} being vapor specific heat at constant volume. The dynamic viscosity formulation is given by Sutherland's[28] law.

$$\mu_v = \mu_{ref} \left(\frac{T}{T_{ref}} \right)^{3/2} \frac{T_{ref} + S}{T + S} \tag{12}$$

Sutherland's constants for water are: $\mu_{ref} = 18.27 \times 10^{-3}$ Pa.s, $T_{ref} = 291.15$ K, $S = 861.11$ K. The thermal conductivity of vapor is a function of temperature and is given by Dincer et *al.*[29] as follows:

$$\lambda_v = \sum_{i=0}^{4} a_i T^i \tag{13}$$

where $a_0 = -7.967996 \times 10^{-3}$, $a_1 = 6.881332 \times 10^{-5}$, $a_2 = 4.49046 \times 10^{-8}$, $a_3 = -9.099937 \times 10^{-12}$, $a_4 = 6.173314 \times 10^{-16}$.

Since the vapor is treated as a perfect gas, the speed of sound is given by the known relation:

$$c_v^2 = \frac{\gamma p}{\rho} \tag{14}$$

where $\gamma = 1.327$ for water vapor, ρ and p are solution of Eq. 1.

Mixture closure equations and phase transition

As mentioned above, the basic hypothesis is that the fluid is in a local thermodynamic equilibrium, hence, at the mixture zone the pressure and temperatures are the same for each phases. To manage mass transfers between phases and therefore the choose of EoS of each phase to compute temperature, pressure and the other thermodynamics properties, an explicit phase transition algorithm based on densities is used. It starts by considering all the variables at the previous time step given by solving Eq. 1, if density is lower than the vapor saturation density then the phase is pure vapor, $\alpha = 1$, EoS of vapor is used. If density is higher than liquid saturation density then the phase is pure liquid, $\alpha = 0$, modified Tait EoS is used. And finally, if density is between the two phases saturation densities then α is given by Eq. 7 and temperature is computed by solving $e = \epsilon e_v + (1 - \epsilon) e_l$, ϵ being vapor mass fraction, the internal energies e_v and e_l are given by EoS of vapor and liquid, respectively, given above. The phase transition algorithm is presented in details in Appendix B. Since the next time step temperature is computed for each phase using the procedure described above, other parameters can be derived such as the mixture viscosity,

$$\mu_m = \frac{1}{\frac{\epsilon}{\mu_v} + \frac{1 - \epsilon}{\mu_l}} \tag{15}$$

and mixture thermal conductivity λ_m which is computed the same way.

One of the advantages of the used approach is that it takes into consideration the physical variations of the pressure since the compressibility of each phase is taken into account. The EoS properly describe the physics of each phase and no modifications of the speed of sound are to be considered (no preconditioning issues are retained). This last point is crucial for the restitution of the real behavior of likely condensation shock waves described further in this paper. On the other hand, the speed of sound drastically varies from phase to other and need to be correctly modeled in the mixture phase. Indeed, the flow presents very low Mach numbers in the pure liquid phase, intermediate in the pure vapor phase and is supersonic in the mixture phase, the sound velocity being very low. In our case, it is expressed following the Wood's relation[30]:

$$\frac{1}{\rho c_m^2} = \frac{\alpha}{\rho_{v,sat}(T)\rho c_v^2} + \frac{1-\alpha}{\rho_{l,sat}(T)c_l^2} \tag{16}$$

Equation 16 takes into consideration the phase transition through the vapor fraction ratio α. The same formulation has been recently used by Saurel et *al.*[31] in the case of a cavitating boiling and evaporating flows.

3. Numerical framework

Finite volume solver: The used finite volume solver is based on Moving Least Squares[32,33] (FV-MLS) approximations. This approach is somewhat different that the usual approach of high-order ($\geq$ 2) finite volume schemes. The usual approach is pragmatic and "bottom-up" . Starting from an underlying piecewise constant representation, a discontinuous reconstruction of the field variables is performed at the cell level. The FV-MLS method starts from a high-order and highly regular representation of the solution, obtained by means of Moving Least-Squares approximation, and it is well suited for general, unstructured grids. This approach is directly suitable for the discretization of elliptic/parabolic equations and high order spatial terms. For equations with a predominantly hyperbolic character, the global representation is broken locally, at the cell level, into a piecewise polynomial reconstruction, which allows to use the powerful finite volume technology of Godunov-type schemes (e.g. Riemann solvers, limiters). A linear reconstruction is used implying a second order space accuracy in our case associated to a Vankatakrishnan slope limiter to manage shocks discontinuities induced by supersonic regimes (see the following section). The reader is kindly referred to works of Nogueira et *al.*[33,34] and Khelladi et *al.*[32] for more details concerning this numerical method.

Low Mach number handling: The disparities between the values of speed of sound into the flow phases are very high. Indeed, the speed of sound is approximatively equal to 1500 m.s^{-1} for the liquid ($\alpha = 0$), 400 m.s^{-1} for the vapor ($\alpha = 1$) and around 4 m.s^{-1} in the mixture ($\alpha = 0.5$). As a result, the compressibility effects based on the Mach number vary in respect to the zone of calculation. Therefore, this issue should be taken into consideration when dealing with numerical flux at very low and very high Mach number calculations. It is widely known that it is difficult to solve the compressible equations for very low Mach numbers using "standard" numerical flux (Roe, Rusanov,...) due to the induced numerical dissipation on the prediction of the pressure, $p \sim M$ rather than $p \sim M^2$. In addition, for an explicit time schemes this induces very small time steps (very restrictive CFL condition). Using preconditioning techniques[35] may overcome these limitations, unfortunately, this implies to modify implicitly the pressure wave propagation dynamics (speed of sound) in the liquid phase which is not suitable in view of the demonstrations projected in the following developments. Consequently, in the present paper, the code does not use any preconditioning. In such a way the authors estimate that the code simulates a better physical behavior of each of the flow phases. A drawback is the need of a very small time step which in our case is around 10^{-7}s using a first order explicit Euler time scheme[31].

Approximate Riemann solver: As mentioned above, the finite volume solver should deal with a large range of wave propagation regimes due to the phase transition mechanisms. The used approximate Riemann solver should then be able to support all-speed regimes. A recent work done by Nogueira et *al.*[36] demonstrates that increasing space order of accuracy to 4th or 5th space orders in addition to the use of a fix of the dissipation term (function of Mach number) of Roe or Rusanov approximate Riemann solvers, for instance, may extend their use to all-speed regimes. For some pragmatic reasons related to the nature of the present investigation, the second order space of accuracy is estimated sufficient. For this reason a modified Simple Low dissipative AUSM solver (SLAU) is used in the present case. The AUSM family solvers are based on the splitting of numerical flux term into convective and pure pressure one. The convective part is decomposed following the procedure proposed by Shima et *al*[37]. The mathematical development is beyond the scope of the present paper. For more details the reader is kindly referred to the work of Kitamura et *al.*[38].

Turbulence handling: In general, a sub-grid scales (SGS) model in a Large-Eddy Simulation (LES) operates on a range of scales that is resolved by discretization schemes. As a result of that, the truncation error of the scheme and the SGS model are mutually linked. The numerical approaches where SGS model and discretization scheme are merged, are called implicit LES (iLES) methods[39]. ILES approach is used in this work. Indeed, to highlight the targeted physical mechanisms related to cloud cavitation shedding and because of the properties of FV-MLS scheme, no turbulence model is used explic-

itly. Turbulence is taken implicitly into consideration through the definition of an adequate number of points in the stencil and the use of appropriate MLS-kernel function parameters in each spatial direction according to Nogueira et *al.*[34,40]. A description of the choice of the best values of stencil morphology and the best kernel parameters are beyond the scope of this paper. For more details and explications, as well as benchmark results, one is kindly referred to references 32–34, and 40.

Computational domain: The computational domain is the axisymmetrical Venturi duct presented in Fig. 1 with 18°/8° convergent/divergent angles, respectively. Its total length is $L = 470$mm. The inlet to throat section ratio is equal to 3. In accordance with experiments, the inlet water temperature is $T_\infty = 300$ K. The saturation vapor pressure in operating conditions is taken $P_{vap} \approx 2200$ Pa. Due to the compressibility of phases, the computational domain is extended (once upstream and once downstream) in longitudinal direction. Velocity inlet and pressure outlet absorbing boundary conditions presented by Schnerr et *al.*[20] are imposed in order to evacuate the non-physical upfront coming pressure waves. The flow velocity at the inlet section ($\mathbf{V_{in}}$) is set to 4 m.s^{-1} and the pressure outlet (P_{out}) is taken equal to 50 kPa. Table I summarizes the boundary conditions.

$\mathbf{V_{in}}$ (m.s^{-1})	P_{out} (kPa)	P_{ref} (kPa)	T_∞ (K)	Re	σ
4	50	85	300	1.2×10^5	1.15

TABLE I. Boundary conditions

The 3D computational domains consists of almost 3.1×10^5 tetrahedral cells. The mesh density is not constant along the computational domain. The convergent/divergent region ($\approx 20\%$ of the overall volume) of the nozzle concentrates almost 80% of the total grid size. This can be considered as sufficient since it presents a pressure loss ratio of approximatively 10% compared to a half grid size and approximatively 2% difference with a 1.75 times larger one (the retained grid is taken as a reference). Depending on the position and the flow regime (time) the local dimensionless wall distance y^+ at the throat region (convergent/divergent) varies from 20 for the lowest value to 300 for the highest value located generally upstream and downstream to the throat zone, which according to the authors is sufficient regarding to the cavitation vapor dimensions and the induced flow structures. Moreover, mass flow rate can be considered as conserved. Indeed, the mean time mass flow rate loss between the inlet and outlet computational domain boundaries is lower than 0.1%.

C. Post-processing and analysis tools

In order to reveal and explore the cavitation phenomenon, a large quantity of experimental and numerical data ought to be generated. As a result, there is a great need to dispose with specific post-processing techniques, such as Proper Orthogonal Decomposition (POD) and wavelet method, which will enable one to extract the synthetic information. This data will be essential to understand, to explore the physical behavior of the flow.

1. Proper Orthogonal Decomposition

Therefore, a POD analysis, based on the intensity of the absorbed light passing through the Venturi nozzle in a series of consecutively taken by a high speed camera images (an experimental data already available in DynFluid Laboratory) and on instantaneous snapshots from numerical simulations, seems to be a reasonable choice.

From a mathematical point of view, the POD is a transformation diagonalizing a given matrix by bringing it into a canonical form, by using a singular value decomposition. More precisely, the POD provides an optimal basis for the model decomposition of an ensemble of data obtained either by experiments or numerical simulations[41]. The gathered information is decomposed into an ensemble of functions, often called empirical eigenfunctions or empirical basis functions, or empirical orthogonal functions. As a result of the optimality of the convergence in terms of a kinetic energy of the POD eigenfunctions, only a small number of modes are necessary to represent the dynamical evolution of the fluid flow. For instance, such a decomposition provides an efficient way of capturing the dominant components in the case of a cavitation flow[42]. Large scale structures, which contain the big part of the kinetic energy of the flow, may be detected and further selected for a reconstruction of the flow dynamics[43].

The coherent structures are described by the deterministic function which best correlates on average with the gathered data set of observations u (data should not necessary be taken at the same physical parameters, for instance at the same Reynolds number[44]). This can be interpreted as the search of function φ that has the largest mean square projection on the observations. The eigenfunctions φ are chosen in order to maximize the average projection of a data field $\mathbf{u}$ on φ. In order to include the statistics the following expression ought to be maximized:

$$\max_{\varphi \in L^2([0,1])} \frac{\left\langle |\left(\mathbf{u}, \varphi\right)|^2 \right\rangle}{\|\varphi\|^2} \tag{17}$$

where $|.|$ is the modulus, and $\langle . \rangle$ may be a spatial or a temporal averaging operation and $\|.\|$ is the L^2 norm defined as $\|f\|^2 = \int_0^1 |f(\mathbf{x})|^2 d\mathbf{x}$. Maximizing the nominator of Eq.17 in some average sense (spatial, temporal)

while keeping the constraint $\|\varphi\|^2 = 1$ leads to the functional:

$$J[\varphi] = \left\langle \| (\mathbf{u}, \varphi) \|^2 \right\rangle - \lambda \left(\|\varphi\|^2 - 1 \right) \tag{18}$$

The choice of the average operator is crucial for the application of the POD analysis. The upper functional is true for all variations $\varphi + \delta\psi \in L^2, \delta\psi \in \mathbb{R}$:

$$\frac{d}{d\delta} J[\varphi + \delta\psi] \mid_{\delta=0} = 0. \tag{19}$$

We can then obtain the integral equation of Fredholm:

$$\int_0^1 \langle u(x)\, u^*(x') \rangle \, \varphi(x')\, dx' = \lambda \varphi(x). \tag{20}$$

For more details about the full mathematical development, one is kindly referred to the PhD thesis of Brenner[45]. The eigenfunctions $\{\varphi_j\}$ produce the optimal basis derived from Eq. 20 using the averaged autocorrelation function $R(x, x') = \langle u(x)\, u^*(x') \rangle$. According to the Hilbert theory, one can assume there is an infinity of orthogonal eigenfunctions associated to the eigenvalues, as a result of the diagonal decomposition of the autocorrelation function. Since the averaged autocorrelation function is $R(x, x') \geq 0$, and Eq. 17 admits a solution equal to the largest eigenvalue of the problem, the eigenvalues λ_j take the following order $\lambda_j \geq \lambda_{j+1} \geq 0$. Each data field u may be reconstructed by using the modal decomposition of eigenfunctions φ_j, as $u(x) = \sum_{j=1}^{\infty} a_j \varphi_j(x)$, where a_j is a reconstruction coefficient defined as $\langle a_j a_k^* \rangle = \delta_{jk} \lambda_j$. In the case where one has information regarding the velocity field, the eigenvalues represent twice the average kinetic energy of each mode φ_j. In such a way, the first eigenvalues correspond to the most energetic modes, hence the most energetic structures. In order to improve the post-processing algorithm and computational time, a snapshot POD method has been used by Sirovich[46]. In the classical POD method , the operator $\langle . \rangle$ stands for a temporal average and $R(x, x')$ stands for a spatial correlation tensor. The use of a snapshot POD makes the size of the eigenvalue problem to be equal to the number of treated images N using $\langle . \rangle$ as a spatial average and a two-point temporal correlation one $C(t, t')$ instead of the spatial correlation in the classic method. In a general manner, when the number of spatial points of data is much greater than the number of treated images, the snapshot POD reduces considerably the necessary computational time for post-processing. As a result, in the present study, the snapshot POD approach will be preferred.

2. *Wavelet Method Analysis*

Wavelet analysis is usually used to decompose time signals into time-frequency space allowing to determine dominant modes of variability through time and, as a result, to associate a dynamic phenomenon to his frequency of occurrence. This method, mainly used in geophysics studies, is particularly adapted to detect near-periodic phenomena as cloud cavitation shedding.

This method, more powerful than classical signal analysis method such as Windowed Fourrier Transform (WTF), has the advantage to be relatively accurate in time frequency localization and also scale independent. Kjeldsen et *al.*[47] are the first to propose the wavelet analysis as a relevant method to measure shedding mechanisms. Brandner et *al.*[48] performed a wavelet analysis in order to extract frequencies of cloud cavitation shedding from a cavity induced by a jet in a cross-flow. In the present paper, the wavelet method developed by Torrence et *al.*[49] is applied to extract the frequencies of appearance of two cloud shedding phenomena which can occur simultaneity. A quick presentation of the method applied to image analysis is developed thereafter.

The method is based on a continuous non-orthogonal wavelet function Ψ_0 which is used in order to perform a complex wavelet transform W_n on a signal scalar serie x_n. After normalization, W_n can be expressed as:

$$W_n(s) = \sum_{n'=0}^{N-1} x_{n'} \sqrt{\frac{\delta t}{s}} \Psi_0^* \left[\frac{(n' - n)\delta t}{s} \right] \tag{21}$$

where s is the wavelet scale, which determine the method precision, δt is the time between two images, N is the number of images and $(*)$ indicates the complex conjugate.

The choice of the function Ψ_0 is here of primordial importance and might be adapted to the study. In the case of image analysis, where the main goal is to extract frequencies of occurrence of some phenomena, a Morlet 6 function is usually used[6,48,49]. The Morlet base, which represents a plane wave modulated by a Gaussian (Fig. 2), is expressed in the time domain analytically as a function Ψ_0 of η, the non-dimensional time,

$$\Psi_0(\eta) = \pi^{-1/4} e^{i\omega_0 \eta} e^{-\eta^2/2} \tag{22}$$

whereas the associated function in the frequency domain, obtained by the Fourrier transform of Ψ_0, can be written as a function of the frequency ω:

$$\hat{\Psi}_0(s\omega) = \pi^{-1/4} H(\omega) e^{-(s\omega - \omega_0)^2/2} \tag{23}$$

where ω_0 is a non-dimensional frequency constant (taken to be 6 for Morlet base[49]) and $H(\omega)$ is a heaviside step function. Both functions are represented below in figure 2.

As a result, using the discrete Fourier transform $\hat{x}_k$ of the discrete sequence of images x_n (where $k = 0...N-1$ is the frequency index) and based on equation 21 and 23, the wavelet transform can be written in Fourrier space:

$$W_n(s) = \sum_{k=0}^{N-1} \hat{x}_k \sqrt{\frac{2\pi s}{\delta t}} \hat{\Psi}_0^*(s\omega_k) e^{i\omega_k \delta t} \tag{24}$$

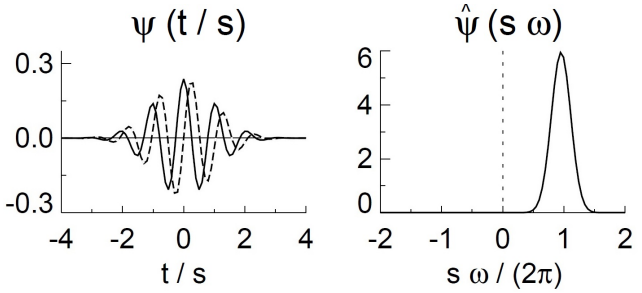

FIG. 2. Morlet wavelet base representation in time domain (left) and in corresponding frequency domain (right). The left plot give the real part (solid) and the imaginary part (dashed) for a wavelet scale $s = 10\delta t$. (From Torrence and Compo[49])

The wavelet transform on the image sequences is estimated with the equation 24 in Fourrier space in order to improve the time calculation. Therefore a Wavelet power spectrum $|W_n(s)|^2$ can be computed and normalized with the variance σ^2. As a result the wavelet method is able to estimate the peaks of Power Spectral Densities (PSD) associated to occurrence frequencies of events and even identify the images corresponding in the sequence.

III. RESULTS AND DISCUSSION

A. Experimental identification of the presence of two shedding mechanisms

In the present study a cavitation regime where two unsteady shedding mechanisms coexist, called "transitory" according to Ganesh[50], is investigated. This regime, studied for a fixed Reynolds number of 1.2×10^5, is observable in the present paper for a small range of cavitation numbers between 1.23 and 1.45. Image sequences, acquired at 1000 frames per second during 3 seconds, are post-processed with normalization and detection of grey levels[5,19].

Classically, the cavity closure length is detected with the maximum of standard deviation on the images[5]. An example of closure detection with image standard deviation is given in Fig. 3. As a result, the non-dimensional transposed length $L^\star$ along the divergent Venturi slope is given in Fig. 4 for top and bottom Venturi nozzles.

One can notice that the evolution of cavity length as a function of the pressure follows the expectations brought by the literature[5,12,21,50]. A wavelet method, developed later in this paper, is applied on cavity closure lines to extract shedding frequencies supposedly associated to the re-entrant jet f_s and to the condensation shock wave f_w. The evolution of these two frequencies as a function of σ is plotted in Fig. 4. A typical spectrum showing the presence of two peaks is plotted in Fig. 5. As previously observed with the position of cavity closure, the two frequencies of shedding appears to follow a certain symmetry on both sides of Venturi nozzles. A low frequency (about 10Hz), which might correspond to the condensation shock wave phenomenon, appears to increase

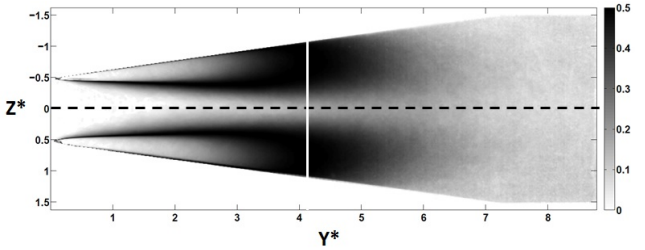

FIG. 3. Standard deviation of the normalized images for a sequence taken at $\sigma = 1.31$. The dotted line divides the study domain in two (top and bottom Venturi nozzle) and the full line, placed at the cavity closure which is almost the same for top and bottom nozzles ($L^\star \simeq 4.05$), is the line for which the grey level is studied for shedding frequency calculations

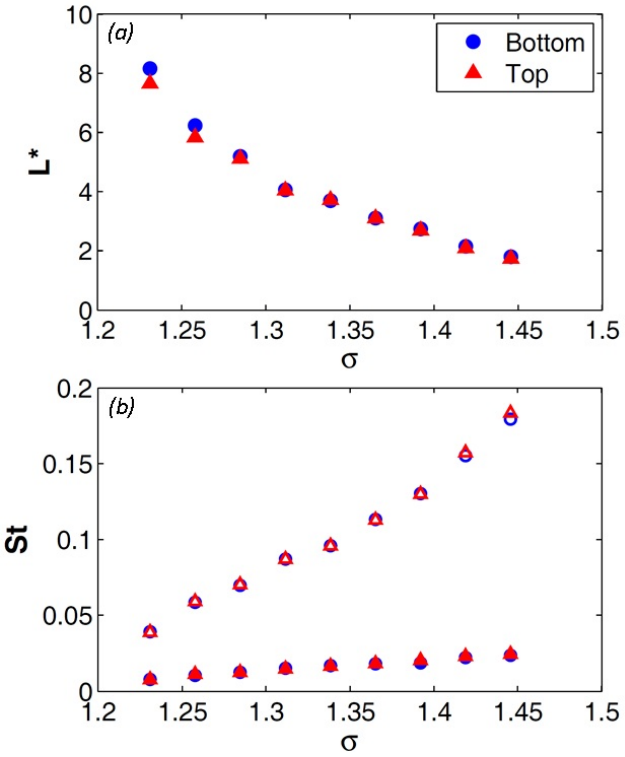

FIG. 4. (Colour online) (Top): Unidimensional sheet cavity length closure $L^\star = L/H_{throat}$ according to the cavitation number σ. Comparison between top (red triangles) and bottom (blue circles) Venturi nozzles. (Bottom): Condensation shock wave (closed symbols) and re-entrant jet (open symbols) shedding frequencies derived from high-speed imaging. Comparison between top (red triangles) and bottom (blue circles) Venturi nozzles

slowly with the pressure whereas the re-entrant jet shedding frequency increases also with the pressure but a lot faster, quadrupling the frequency between $\sigma = 1.23$ and $\sigma = 1.45$. An explanation would be that the re-entrant jet is highly influenced by the cavity size, the phenomenon occurring with more difficulty for longer cavities. For low cavitation numbers ($\sigma = 1.20$ and 1.23), a difference between top and bottom Venturi sides can be noticed.

In order to highlight the two shedding mechanisms,

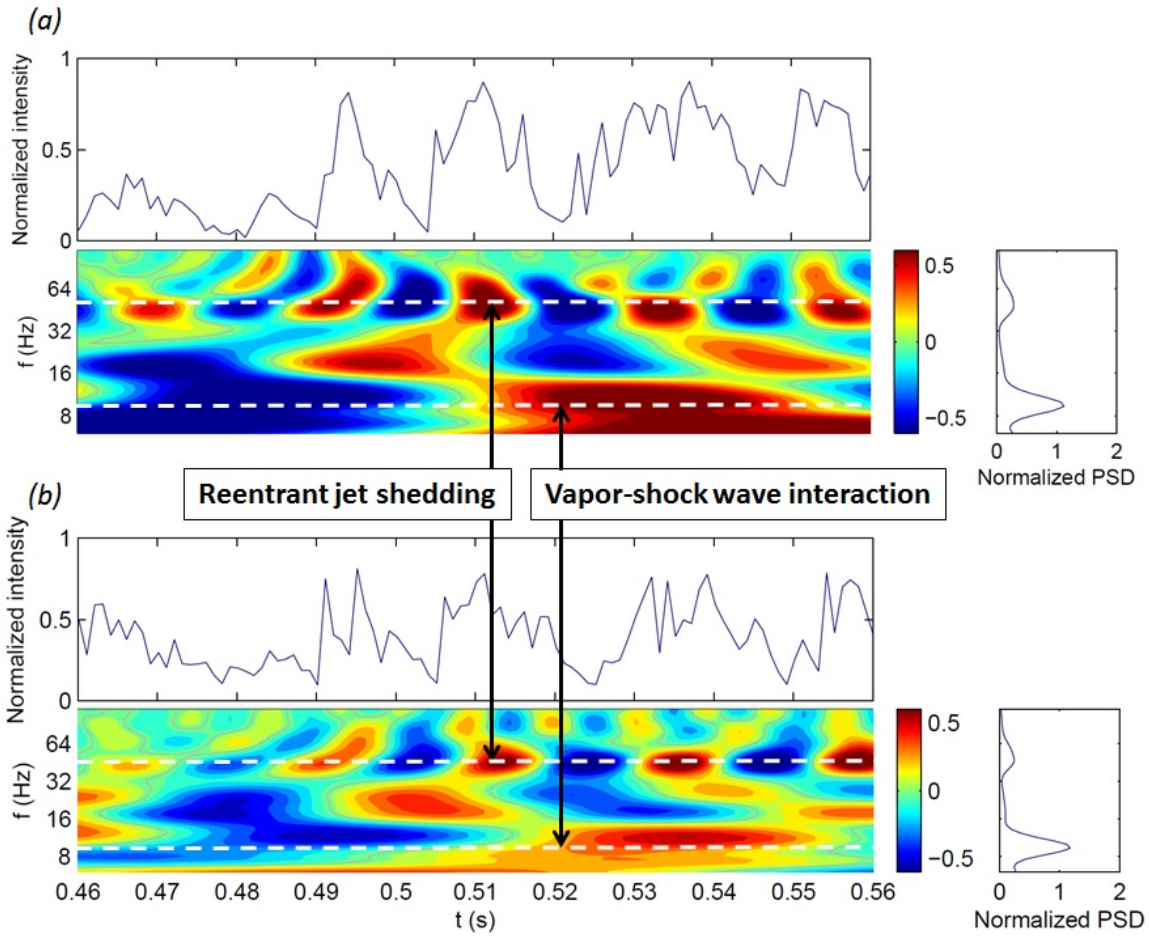

FIG. 5. (Color online) Time series of grey level taken at cavity closure between 460 and 560 ms of the image sequence for $\sigma = 1.23$ and corresponding wavelet transformation for (a) top and (b) bottom Venturi nozzles. Power spectral density is obtained from the wavelet transformation (normalized by the variance). The re-entrant jet shedding identification corresponds to the last image of Fig. 10 taken at 512 ms whereas the vapor-shock wave, taken at 520 ms corresponding to the beginning of the associated shedding cycle, is presented in Fig. 17

the choice is made to focus the present study on the extreme case, that is $\sigma = 1.23$ where a lot of dynamics and features might be encountered. Indeed this case has the advantage to deal with cavities of big size where shedding mechanisms might be easier to observe. Moreover, in this case, the condensation shock wave seems to be a phenomenon particularly pronounced and both numerical and experimental investigations might give more relevant results.

Wavelet method, is used in the experimental case $\sigma = 1.23$ where the two shedding phenomena are clearly observed. The method is applied following the steps given thereafter. First, the images are divided in two in order to study separately the top and the bottom Venturi nozzles. Secondly, according to Danlos et *al.*[5], the evolution of grey level is studied at the cavity closure, where standard deviation on the image sequence is maximum, selecting the vertical line going through this point as presented in Fig. 3. Finally wavelet Power Spectral Densities (PSD) $|W_n|^2$ is calculated from the grey level signals as well as the wavelet transform. Wavelet analysis results about the shedding mechanisms, illustrated in Figs. 10 and 17, are exposed in Fig. 5.

As a result, frequencies of shedding phenomena can be identified with corresponding wavelet PSD peaks. The cloud cavitation due to re-entrant jet, for which a cycle is highlighted in Fig.10, presents the lower PSD peak at a frequency $f_s = 47.2$ Hz for the bottom Venturi and $f_s = 46.7$ Hz for the top Venturi nozzle. Meanwhile, the shedding induced by the vapor-shock wave, which is illustrated in Fig. 17, occurs at a frequency $f_w = 9.5$ Hz on both sides. The different outcomes obtained with image analysis and their uncertainty (by evaluating the effect of image processing and the wavelet method) such as frequencies of shedding, wavelet PSD peaks ratio associated $R_{PSD} = |W_n(f_w)|^2/|W_n(f_s)|^2$ and cavity closure length along the Venturi profile are reported in Table II.

One can notice looking either grey level signals, wavelet transforms (Fig. 5) or shedding frequencies that there clearly exists a symmetry of the upper and down cavities as concluded previously by Tomov et *al.*[51]. The bubbly shock wave appears to be in that case the dominant mode

of cloud shedding in comparison with the re-entrant jet. However in this particular case, where cavities are long enough, the symmetry seems to begin to break. Indeed, as previously noticed, a difference between top and bottom Venturi cavity lengths and re-entrant jet frequencies can be seen. The $2D$ observations do not permit to interpret this symmetry break-up. On the other hand, $3D$ simulations could reveal such a dynamical feature.

B. Comparison of global features with POD techniques

This section presents the application of the POD on series of vapor fraction consecutive images taken from the numerical simulations. The POD is used as a complementary technique to study the different cavitation regimes. The side view images are taken at three different equally spaced locations on the Venturi nozzle: the front, the middle and the back. For each location a total number of 1200 images are extracted. By definition, the optimal basis is given by the eigenfunctions φ_j of Eq. 20. In the present study $u(x)$ is the vapor fraction, hence the eigenfunctions φ_j play the role of a "weight" for the reconstruction of the flow. Moreover, if $u(x)$ represents a velocity field, φ_j would have been a kinetic energy.

A convergence study allows to determine the number of snapshots necessary to validate the decomposition. Figure 6 presents the contribution of the first four modes j in the reconstruction of instantaneous images obtained by the decomposition of $N = 1200$ snapshots.

The analysis shows that $N = 900$ snapshots are sufficient for the decomposition to obtain converged results. As a result, the same curves for $N = 900$ for the back face at $\sigma = 1.15$ will not be presented. All the modes are calculated for $N = 900$. For more details regarding the post processing technique the reader is kindly referred to the works of Danlos et *al.*[42] and Tomov et *al.*[51].

One can notice the peaks at the energy contributions in Fig. 6 at the vicinity of $N = 300, 500$ and 700 snapshots, which might correspond to the instants of condensed shocks that are taking place. It can be seen in the energy decay for mode 0, that the number of images between the second and third peaks are almost constant, which is not the case for the first one. One possible explanation is the fact that the first condensed shock takes place after the cavity reaches its full length. This is clearly not the case once the shock waves start to propagate and influence the production of vapor at the Venturi nozzle.

	Bottom Venturi	Top Venturi	Uncertainty
f_s (Hz)	47.2	48.7	±4%
f_w (Hz)	9.5	9.5	±4%
$L^\star$	8.16	7.65	±2%
R_{PSD}	4.76	3.90	–

TABLE II. Experimental results for $\sigma = 1.23$

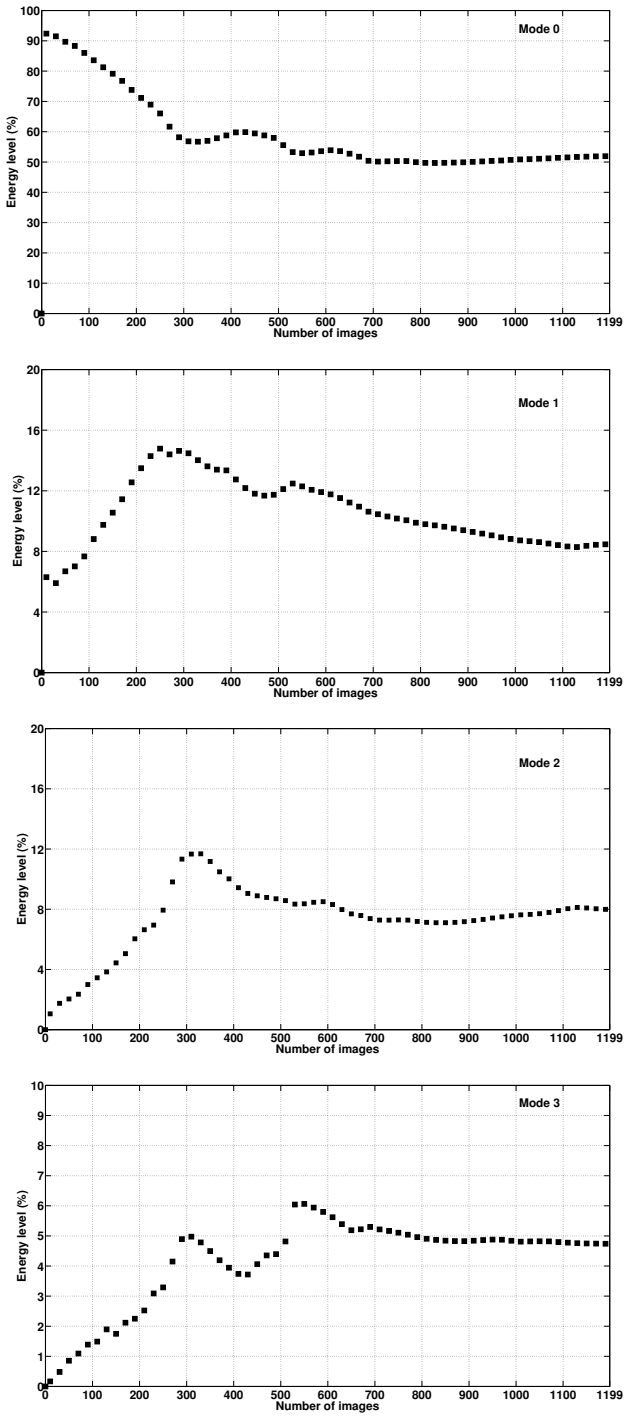

FIG. 6. Convergence study for case (a) applied for the back surface of the Venturi nozzle for the first four modes j in the reconstruction of instantaneous images obtained by the decomposition of $N = 1200$ snapshots. It can be seen that the energy contribution of the 4^{th} mode is almost negligible

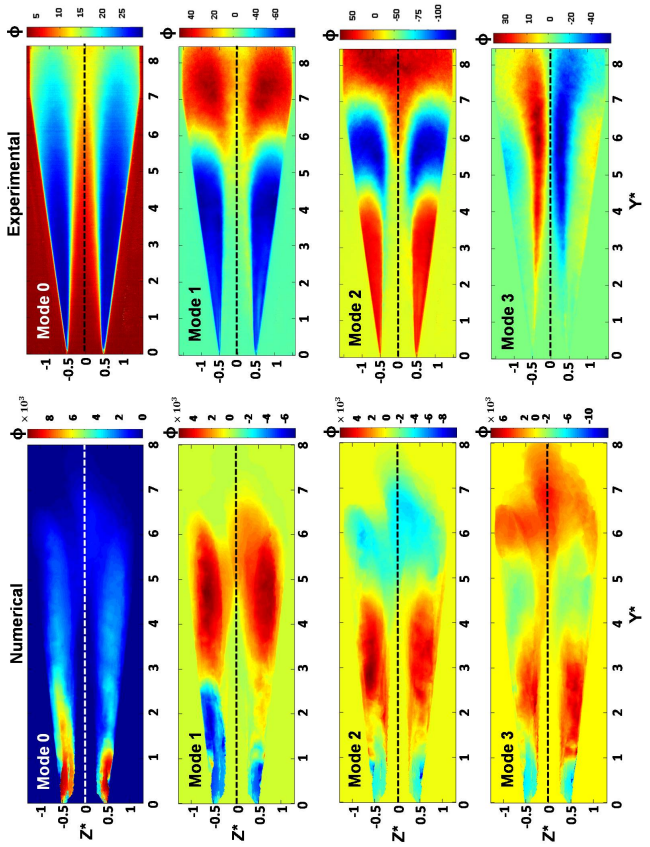

FIG. 7. (Color online) (Left): POD on side view images at superimposed numerical data, (Right): POD on side view images from experimental data

In order to compare the experimental and numerical POD modes, one would need to deal with superimposed side view numerical snapshots, nevertheless the relatively small number of cavitation cycles data gathered from the simulations. According to the authors, the vapor structures may not necessarily lay in the same spatial plane, as it is the case in experimental side views.

As a result, Fig. 7 illustrates POD modes of numerically superimposed snapshots and experimental ones. It can be observed that the lengths of the cavitation vapor are comparable for modes 0. Moreover, the advected vapor structures are symmetrically spread for both couples of modes 1 and 2. One can notice the likelihood for the vapor characteristic length to be in the range of $6\mathrm{H}_{throat}$ to $7\mathrm{H}_{throat}$ for the numerical case and $7\mathrm{H}_{throat}$ to $8\mathrm{H}_{throat}$ for the experimental one.

In order to take into consideration the possible $3D$ effects, the first four modes extracted from numerical data are presented in Fig. 8 for $\sigma = 1.15$. The values of the energy contributions per mode and per plane are given in Table III. It can be seen that the values per mode are comparable for all of the cases. A brief discussion about the POD application on numerical data is firstly provided, followed by a discussion on the experimental POD modes.

The energy contributions of the first four numerical modes contribute to almost 100%, as it can be seen from Table III. For each plane, modes 0 account for slightly

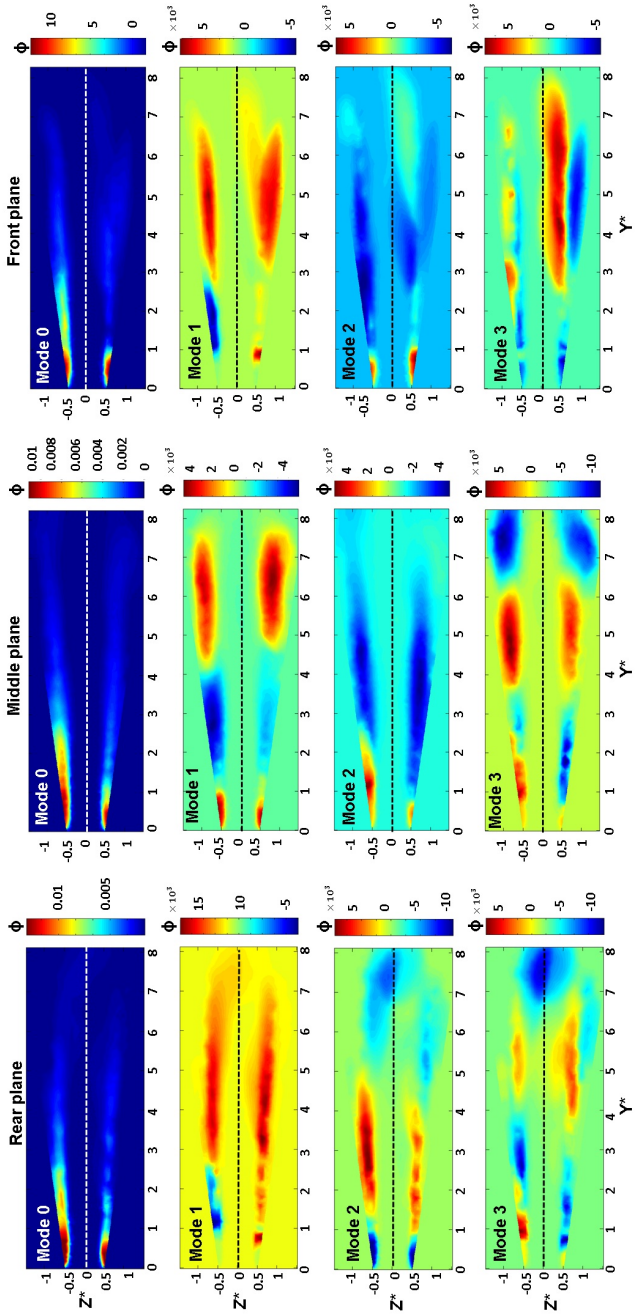

FIG. 8. (Color online) The first four numerical modes for each plane location at $\sigma = 1.15$. The dashed line represents the horizontal line of symmetry

Plane	Mode 0	Mode 1	Mode 2	Mode 3	Total
Front	90.71	7.65	1.21	0.24	99.84
Middle	92.50	6.19	0.94	0.19	99.82
Rear	92.38	6.29	1.05	0.17	99.89
Experiment	89.45	5.75	1.45	0.30	96.95

TABLE III. Energy contributions per mode [%]

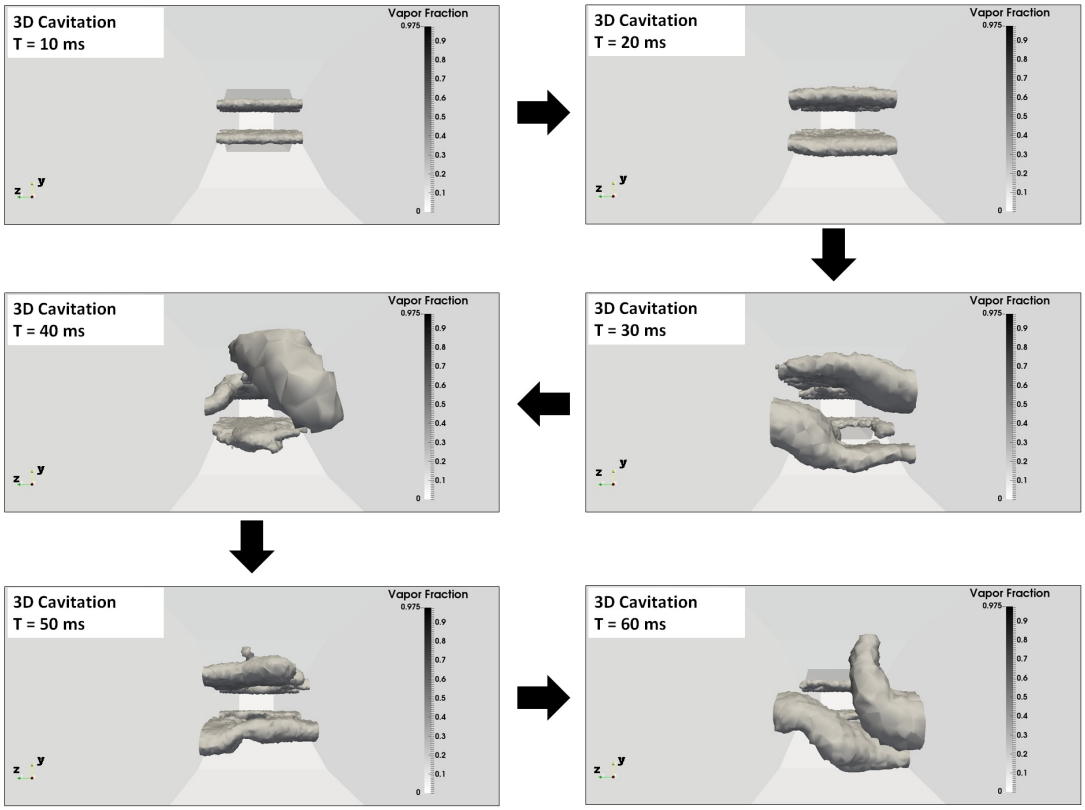

FIG. 9. A back view of the dynamics of the numerical cloud cavitation for $\sigma = 1.15$ with a time step of 1×10^{-7}s. The snapshots are taken with a time interval of 10 ms

more than 90% and modes 1 contribute with values of the order of 6 to 7%. Those values are higher than the level of 1%, which was reported by Danlos et *al.*[42] as a sign of the presence of a cloud cavitation. A similar observation can be made for each of modes 2, where the values range in the vicinity of 1%. The energy contributions of all of the fourth modes are insignificant. It can be seen from Fig. 8 that the spatial distribution of mode 0 is almost symmetrical with respect to the horizontal axis. The vapor phase stays continuous for the middle plane, which is not the case for the front one. The explanation lies in the fact that the side-entrant jet plays an important role in the flow dynamics near the wall. Its influence is much less visible in the case of the rear plane. It can be seen that modes 1 are symmetrically spread in respect to the horizontal dashed line. The advected vapor is presented by the dark zones, which have very similar lengths for the middle and front planes. One can recognize the twist form of the advected vapor at the rear plane at $Y^* = 6$ to $Y^* = 8$ for mode 1 (see Fig. 9). Similar dynamical behavior can be found for modes 2, where a symmetrical spread is visible for the rear and middle cuts. The most stable and symmetric flow is the one on the middle plane.

The energy contribution values of the experimental POD modes are similar to the numerical ones, as it can be seen from Table III. The energy value for mode 1 is higher than 1% and could be considered as a sigh of a cloud cavitation existence. The symmetry of the flow can be clearly observed for all of the modes, which implies synchronous behavior on each side of the Venturi nozzle. The latter confirms the visual observations from the instantaneous snapshots. A possible physical interpretation for each of the four modes can be as follows. Mode 0, as a major contributor to the decomposition, can be an indicator of an oscillating cavity, if one is not interested in the other modes. The dark zones from $Y^* = 6$ to $Y^* = 8$ for mode 1 and from $Y^* = 5$ to $Y^* = 7$ can be interpreted as advected vapor structures. The last mode 3 might be seen as the weak interaction between the top and bottom cavitation vapor before a separation to take place. A typical representation of such an interaction can be seen at the instantaneous snapshots for T= 508 and T= 510 ms in Fig. 10.

To conclude the POD analysis confirms the global symmetry of the two sided cavities in both experimental and numerical data. The number of cycles in experimental case is higher than in simulations, which leads to more significant results. However, some $3D$ effects appears to have an important role in the two shedding mechanisms and, as a result, numerical simulations appear to be necessary to illustrate these different features.

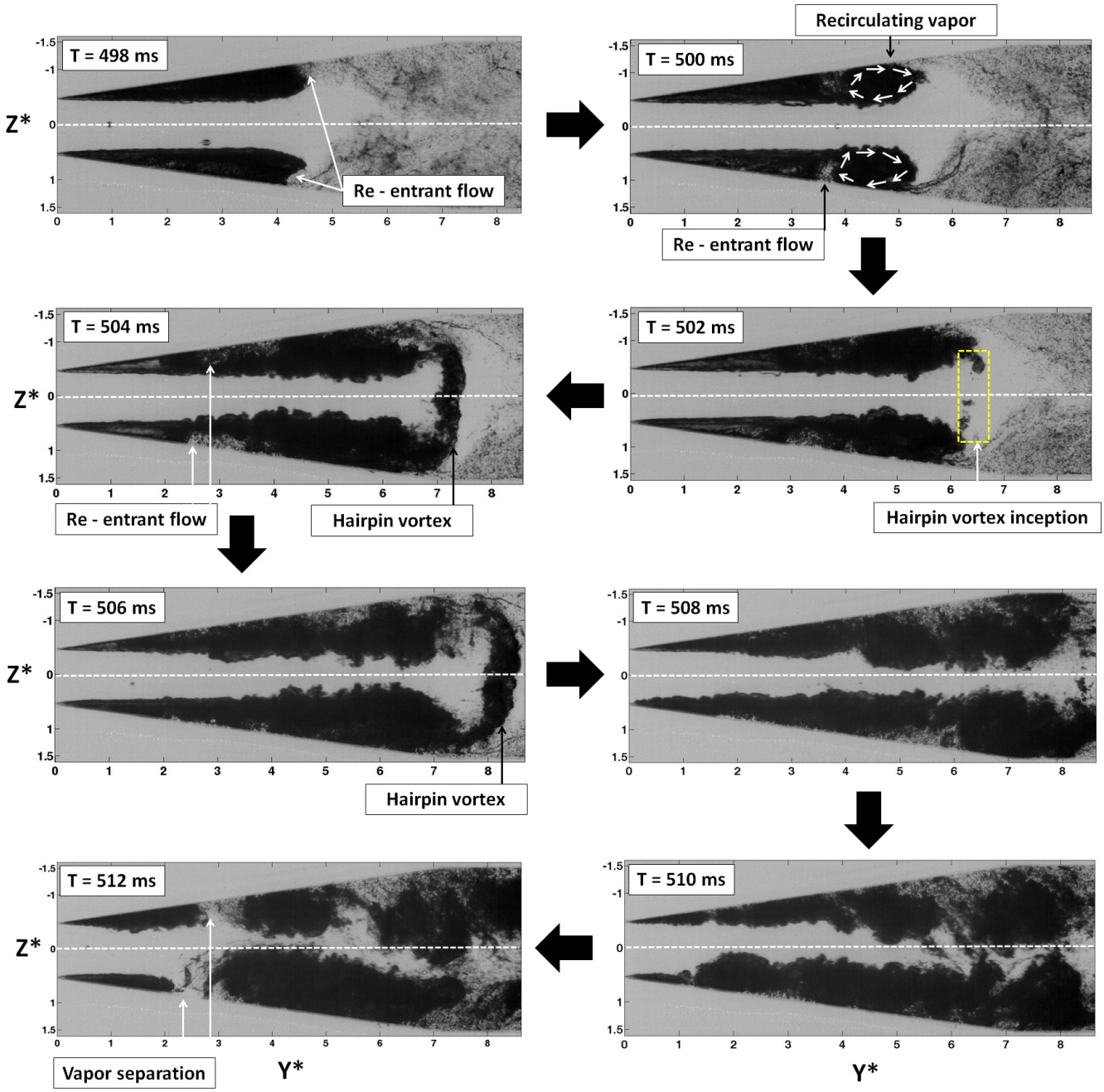

FIG. 10. Normalized instantaneous snapshots from high-speed image series showing the re-entrant jet dynamics for $\sigma = 1.23$. The images are taken in the total sequence between 498 and 512 ms with $\Delta t = 2$ ms. The horizontal symmetry is shown in white dashed line. The re-entrant jet appears at the same instant on the top and bottom side of the nozzle. It flows upstream the flow, while creating recirculating vapor zones and a hairpin vortex. It is then advected by the flow and a vapor separation takes place

C. Re-entrant jet shedding

As previously explained in Sec. II, the re-entrant jet is a well known shedding mechanism observed[9,10,15] and characterized[5,12,50] in several studies. The cycle illustrated in Fig. 10 consists of the following steps: first, the cavity grows from the Venturi throat and a re-entrant jet appears at the sheet cavity closure. Secondly, it flows upstream on the wall and eventually cuts the formed vapor. In general, the re-entrant jet is created by the flow by an expansion of its closure region. In such a way and in a combination with the Venturi wall, a stagnation point is created. The conservation of momentum makes the fluid to pass beneath the cavity, hence the jet progresses and results in a vapor separation[52]. As a result, a cloud is formed and is further advected. The cloud va-

por collapses in the divergent Venturi nozzle zone where the pressure is higher than the one at the throat section. In such a way, the cavity length is reduced and the whole process repeats itself. The repeatability of the process is characterized by the shedding frequency f_s. In the present section, the re-entrant jet shedding dynamics are pointed out with wavelet grey level analysis (see Fig. 5). Afterwards, the numerical simulations are introduced and a comparison is made with experimental data.

Figure 10 shows the multiphase flow dynamics in experimental conditions for $\sigma = 1.23$. A sequence of normalized instantaneous snapshots in Fig. 10 are presented in order to illustrate the re-entrant jet dynamics. Its development can be seen at the closure region on both sides of the nozzle. The re-entrant jet travels upstream the flow and it creates two recirculating vapor zones. Furthermore, one can see the clouds cavitation expansion and the creation of a hairpin vortex. It plays the role of an interaction between the top and bottom divergent sides of the nozzle. The re-entrant jet continues to travel upstream, while the hairpin vortex is advected by the flow until vapor separation. The wavelet transform associated to the sequence (Fig. 5) show that the vapor separation occurring at 512 ms correspond to a peak of wavelet power spectrum for both Venturi nozzles at a frequency $f_s \simeq 48$ Hz (see Table II). As a result, the re-entrant jet dynamic is well-characterized experimentally in two dimension with a frequency of occurrence f_s, however numerical simulations are required in order to see possible 3D effects.

The 3D cavitation simulation is presented hereafter. The Mach number varies from 2.44×10^{-4} to 2.89. The maximum value of the flow velocity at the Venturi throat is equal to 13.60 m.s^{-1}. Figure 11 represents the velocities in each spatial direction at $T = 20$ ms. The presence of the re-entrant jet is well visualized on the left image. The horizontal velocity field is presented at three different planes at a distance $L = [3H_{throat}, 5H_{throat}, 8H_{throat}]$. One can see that the value of the vertical component of the velocity is symmetrically distributed in respect to the horizontal axis. It is interesting to note the presence of a side-entrant jet in the transverse velocity distribution on the right image in Fig. 11. The transverse plane passing through the top vapor zone shows that the side-entrant jet has the same velocity on the near and far sides of the Venturi nozzle. This is not the case on the bottom, where the velocity component on the near side is twice the one on the far side of the nozzle. Such a difference creates an interesting dynamics presented in Fig. 12 wher the evolution of the vapor phase is presented by a sequence of snapshots.

As it can be seen at $T = 10$ ms, the two vapor zones are clearly symmetrical. One can notice the development of the vapor rupture which starts from the Venturi walls and evolves to the middle section. Such a dynamical behavior has been observed by Schneer et *al.*[20] and Foeth et *al.*[53] in the case of a hydrofoil and by Dular

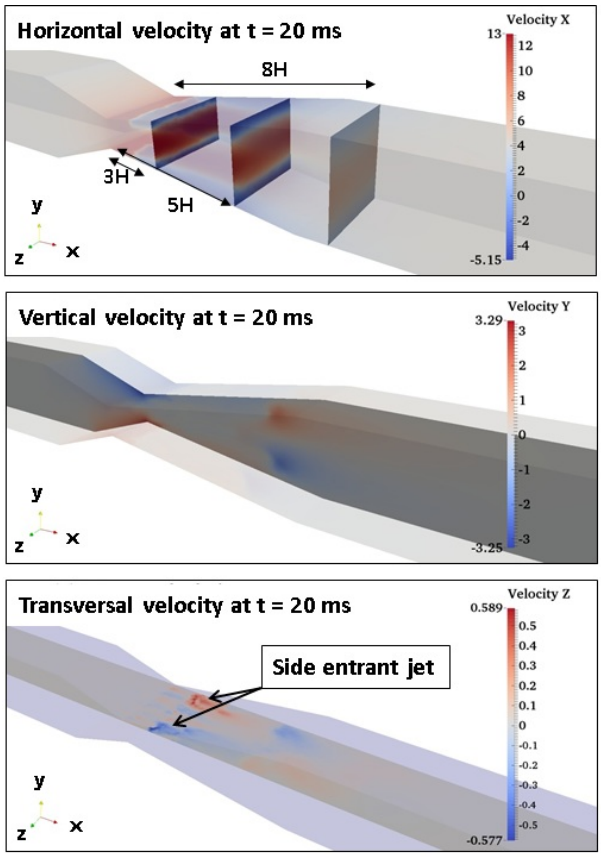

FIG. 11. (Color online) Numerical results for $\sigma = 1.15$: horizontal, vertical and transversal velocities distribution at $T = 20$ ms. The existence of re-entrant and side-entrant jets is visible

et *al.*[13] in the case of Venturi nozzles for small but wide throat sections. This phenomenon can be defined as a "side-entrant jet". At $T = 20$ ms the rupture increases, but a cloud separation is still not present. The rupture zones are symmetrical in respect to the horizontal axis. At $T = 30$ ms the separation has already taken place and the two clouds are advected by the flow. One can note that the vapor starts to follow a spiral trajectory. The cloud vapor at the upper left corner and the bottom right one evolve symmetrically and bond with each other as it is presented at $T = 40$ ms. In the mean time the vapor at the throat increases and a new cloud separation takes place at $T = 50$ ms. The spiral movement is again presented at $T = 60$ ms where the two advected clouds are about to get into contact. Figure 9 shows a front view of each of the snapshots in the sequence. It clearly illustrates the vapor spiral movement. The length of the clouds before their complete separation is equal to $6.4H_{throat}$. The two clouds are synchronized and the separation takes place at the same time on the top and bottom sides of the Venturi nozzle.

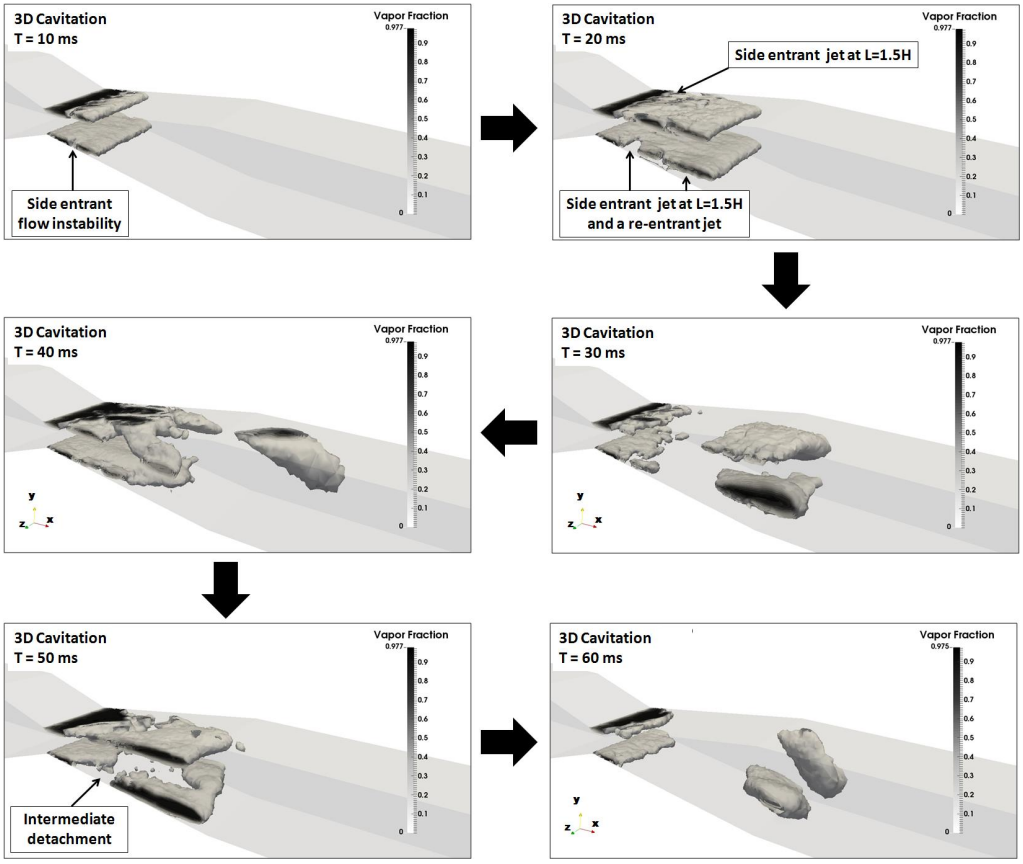

FIG. 12. Cavitation sequence from numerical simulation for $\sigma = 1.15$: $\mathbf{V_{in}} = \mathbf{4}$ m.s^{-1}, $P_{out} = 50$ kPa, time step of 1×10^{-7}s. The snapshots are taken with a time interval of 10 ms

D. Condensation shock wave shedding

Under certain flow conditions the cavity is not very dense and the local speed of sound becomes very small. As a result, high local Mach numbers can be reached. In that sense the time scale changes, which inevitably leads to a change in the flow physics. Low values of the speed of sound result in a slower propagation of any potential disturbances in vapor than in liquid. This leads to a presence of shock waves at the end of the cavity that can induce a massive cloud cavitation shedding. In the present section, the condensation shock wave dynamic is observed and explained with numerical simulations. Some experimental images are provided as illustrations.

The bubbly shock wave has been studied experimentally with X-ray in the PhD work of Ganesh[50]. It has been found that a second type of shedding mechanism, which corresponds to a propagating discontinuity is present and can affect the vapor cloud shedding of the Venturi nozzle. Very similar dynamical behavior is observed numerically in the present case study, in the time frame between 40ms and 50ms illustrated by eight snapshots in Fig. 13.

Shortly after $T = 40$ms, a backward cavity motion is observed due to the implosion of the first advected vapor clouds. Indeed, some small quantity of vapor is detached and suddenly the cavity length starts to contract and decreases without any advection or another separation to take place. The transition is extremely rapid, as it can be seen in Fig.13, where the time step between snapshots is taken as 1ms. The contraction process is equally presented on the top and on the bottom side of the divergent part of the nozzle. As a result, the decrease of the cavity length is synchronized and symmetrical in respect to the horizontal axis. It can be seen that one part of the vapor cavity starts to detach somewhere at its middle length. As a result, a separation is present followed by an advection. Such a dynamical behavior is quite interesting and corresponds to the one described by Ganesh et *al.*[54] condensed shock dominant shedding mechanism. This scenario is somehow different compared to the existence of a stagnation point and the formation of a re-entrant jet at the rear of the vapor cavity. The liquid is in a cinematic equilibrium when a re-entrant flow is responsible for the shedding, while in the present observation the contraction starts at the moment when the first advected clouds disappear.

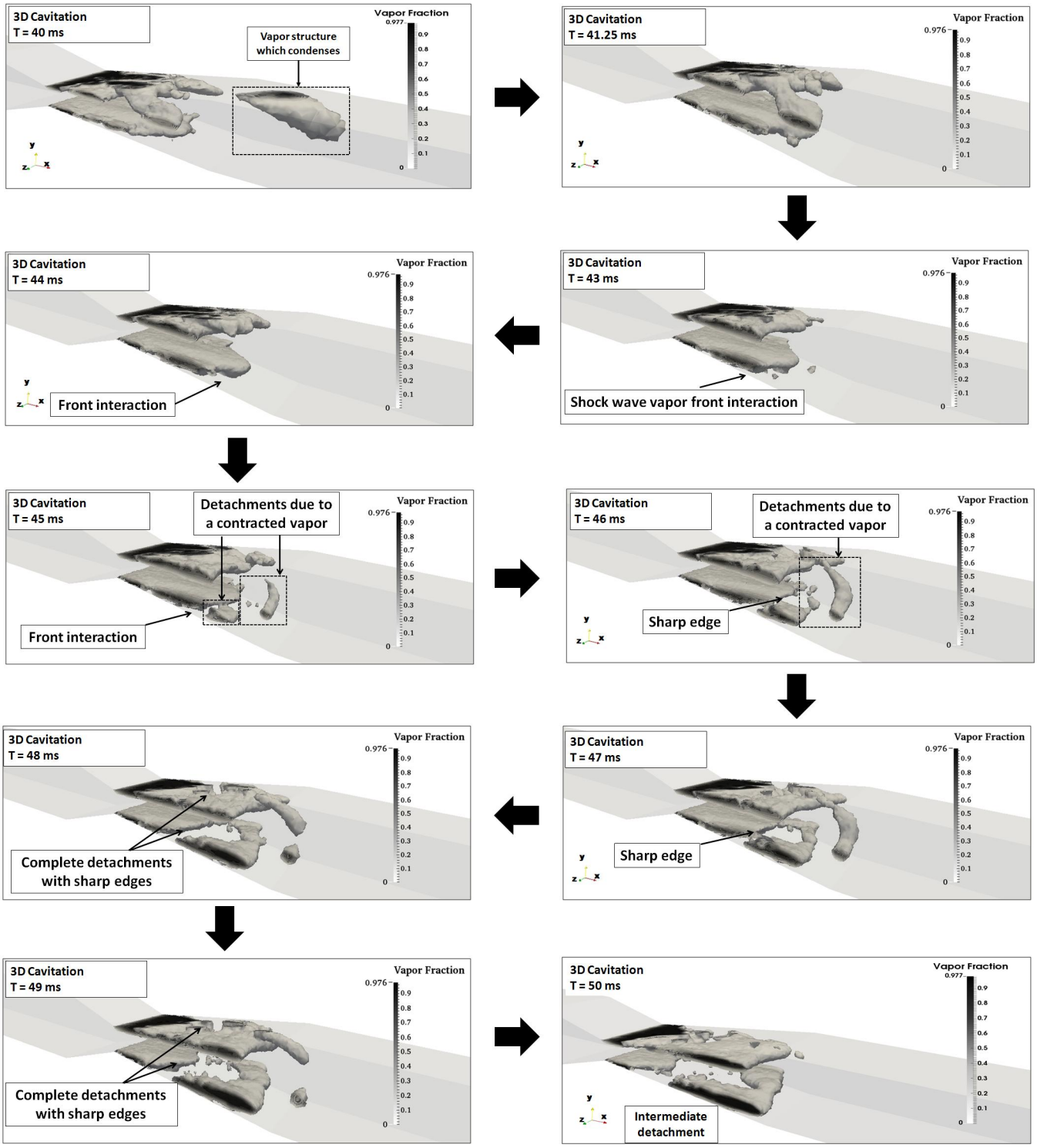

FIG. 13. Vapor fraction dynamical behavior in the presence of condensed shocks at the cavity closure regions. The ten snapshots present the time interval starting at T= 40 ms and ending at T= 50 ms

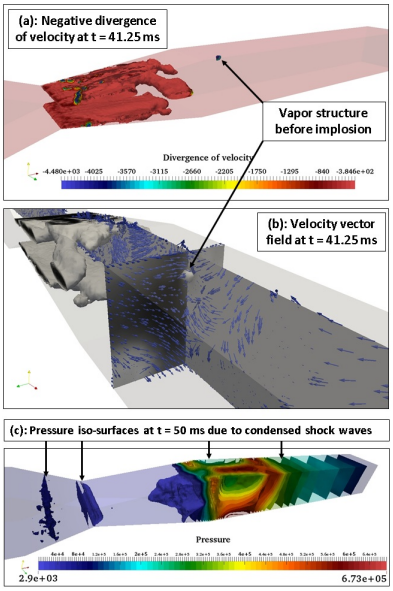

FIG. 14. (Color online) Numerical representation for cavitation at $\sigma = 1.15$, (a): the divergence of the velocity at $T = 41.25$ ms, (b): velocity vector field on two plane cuts passing through the implosing vapor structure and (c): the pressure field at $T = 50$ ms by thirty iso-surfaces. The corresponding snapshots of the vapor volume fraction can be seen in Fig.13

Figure 14 illustrates the pressure field at the moment of implosion of the first advected vapor. It can be clearly seen that a value of 673 kPa is reached at the location of the implosion. As a result of the collapse, the pressure waves are propagated in each direction, which brakes the spatial development of the vapor phase and it changes rapidly its dynamical behavior. The contraction of the vapor phase does not lead to an apex pinch-off in the presented case study. The same phenomenon is constantly repeated when the advected vapor structures collapse down the flow and increase sufficiently the pressure. Four cycles of cavitation shedding are observed. The length of vapor clouds at the end of the fourth cycle is drastically reduced compared with their lengths before the first shedding to take place. At $T = 41.25$s it is roughly equal to $6H_{throat}$, while at the end of the fourth cycle L is equal to $2H_{throat}$. The local Mach number at the spatial location of the collapse for $\alpha \approx 0.1$ is of the order of 1.1 and the local value of the speed of sound decreases to 10 m.s^{-1}. These values are consistent with the data described by Brennen[55] and recently experimentally reported by Ganesh et *al.*[50,54]. Moreover, the divergence of the velocity is a clear indicator of the condensation process, which takes place. As it was recently pointed out by Mihatsch et *al.*[56], a negative value of div($\mathbf{u}$) is proportional to the vapor production rate, as long as the thermodynamic state corresponds to a two-phase mixture. Figure 14 presents the instant at $T = 41.25$ ms, where a negative div($\mathbf{u}$) is clearly visible. Neglecting any dissolved gas content, the surrounding liquid near the advected vapor structure, accelerates towards its center, until a condensation is reached as a last stage of the collapse process. As a result, the pressure increases until a collapse takes place, as it is shown in Fig. 14. The upper described dynamics follows closely the one described by Mihatsch et *al.*[56].

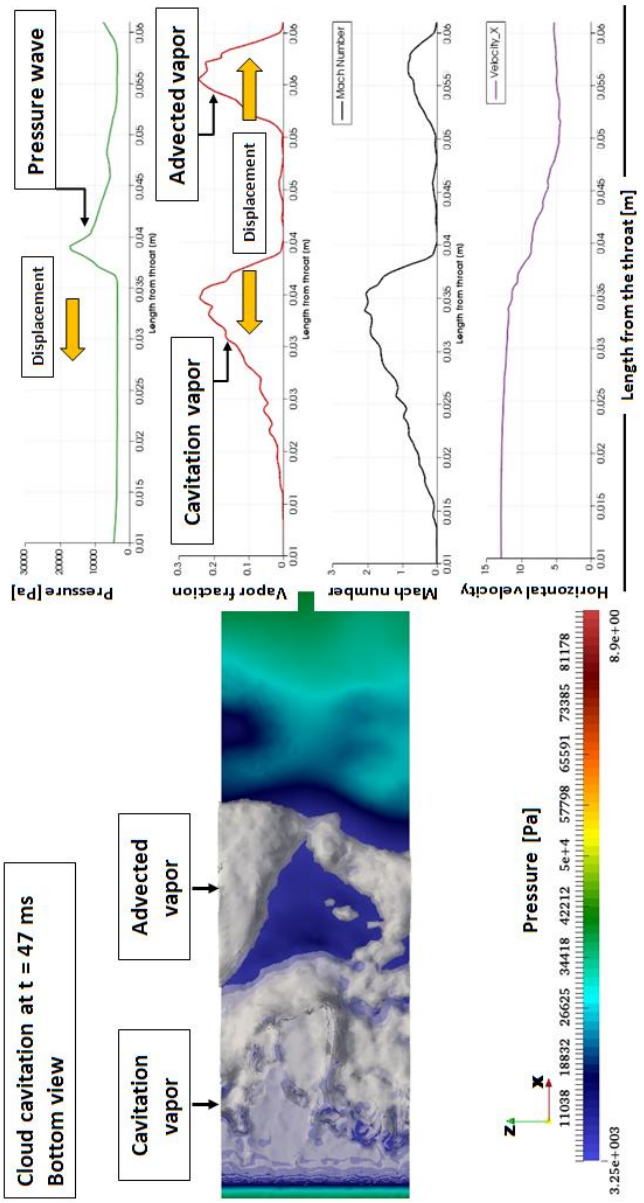

FIG. 15. (Color online) A bottom view of cloud cavitation from a numerical simulation at $\sigma = 1.15$ (left). The pressure, the vapor fraction, the Mach number and the horizontal flow velocity are plot in terms of a distance from the nozzle throat (right). The plots are extracted along a line following the bottom divergent zone. The two vapor fractions are moving in opposite directions. The time interval starts at T= 40 ms and ends at T= 50 ms. The multimedia view corresponds to the sequence shown in Fig. 13. (Multimedia view)

It is interesting to show the spatial evolution of the pressure wave and the consequence on the vapor fraction, the local Mach number and the horizontal velocity component, in order to exclude any influence of the re-entrant jet. Figure 15 illustrates the shedding cavita-

tion seen from the bottom, as well as the corresponding evolution of the pressure wave. It can be seen that the wave moves in an opposite the flow direction. At a certain moment, the vapor fraction is cut by the wave into two smaller structures. Each one of them moves into opposite directions. The Mach number reaches local values of of the order of 3. The horizontal component of the flow velocity stays constantly positive which implies that no re-entrant jet effects are present. For more details the reader is kindly advised to see the supplementary material at Fig. 15. A value of 5.02 m.s^{-1} for the shock wave velocity propagation is estimated (for a time period of 3.5×10^{-3}s the shock wave moves forward at 1.76×10^{-2}m). The obtained velocity has the same order of magnitude and fits in the range of values given by Ganesh[50].

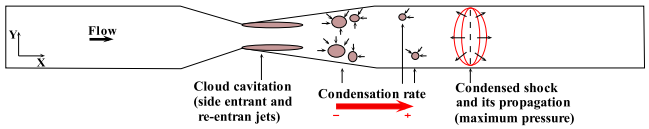

FIG. 16. (Color online) An illustration (not to scale) of the mechanisms governing the vapor dynamics in the present case study. The maximum condensation is achieved just before the vapor structure collapse and the maximum pressure is reached at the vapor collapse

As a result, the cavity dynamics is governed by three different phenomena shown in Fig. 16. The first one is the re-entrant jet, the second one is the side-entrant jet and the third one is the shock wave due to the collapse of the advected vapor structures.

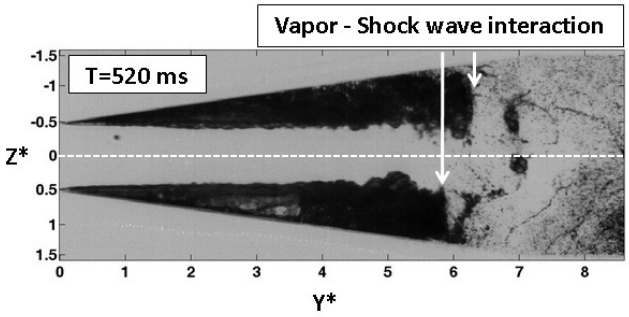

FIG. 17. Normalized instantaneous snapshot (taken at t = 520 ms, following the sequence show in Fig. 10) showing the vapor-shock wave interaction for $\sigma = 1.23$. The existence of sharp edges might be due to the propagation of condensed shock waves. The vapor fraction experience the "water-hammer" effect

An experimental illustration of a back-flow propagating condensed shock wave is shown in Fig. 17. The normalized instantaneous snapshot taken at $\sigma = 1.23$ clearly presents the vapor-shock wave interaction. One can notice the sharp edges at the cavity closure region on both sides of the Venturi nozzle, as a result of the propagating wave. At the same instant some small vapor structures are detached and continue to be advected by the flow. Very similar sharp edges have been observed also by Ganesh[50] in his PhD work.

The propagation of pressure waves is a rapid phenomenon, which makes it not straightforward for a visualization. According to Ganesh et *al.*[54], its visibility is highly dependable on the cavitation number. Moreover, a sampling frequency of 1 kHz for the high-speed camera does not necessary guarantee the possibility to properly capture a complete sequence of images showing an interaction between cavitation vapor and pressure waves. As a result, Fig. 18 shows a shock wave influence on shedding cavitation for a slightly higher $\sigma = 1.31$. One can clearly see that at $L = 3.8H_{throat}$ sharp edges are formed at the cavity closure region. As a result, a synchronized double vapor detachment is obtained on each side of the nozzle. It is visible that an upstream propagation of a shock wave changes the cavitation shedding mechanism.

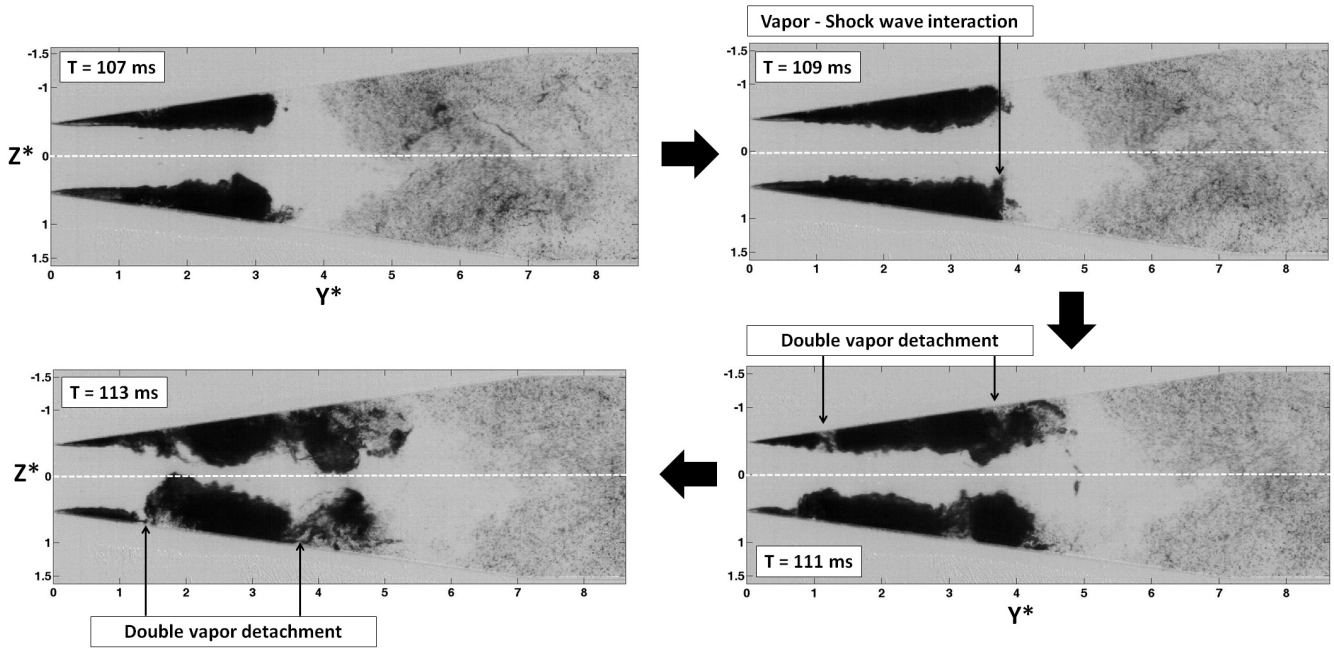

FIG. 18. A sequence of normalized instantaneous snapshots from $T = 107$ ms to $T = 113$ms showing the vapor-shock wave interaction for $\sigma = 1.31$ at Δt between the images of 2 ms. The horizontal symmetry is shown in white dashed line. A sharp edge is visible as a result of the vapor-shock interaction.

IV. CONCLUSIONS

In the present paper, "transitory" cavitation regime has been investigated numerically in 3D and experimentally in 2D. For a constant inlet flow, a small range of cavitation numbers, where two cloud cavitation shedding mechanisms coexist, has been studied experimentally. A classical evolution of cavity closure position as a function of cavitation number has been observed and two frequencies of cloud shedding, increasing with the cavitation number, have been highlighted. The choice has been made to focus only on one case with a corresponding cavitation number $\sigma = 1.23$ in order to study the dynamics of the two-phase system.

The use of a "full" $3D$ compressible code is justified by the fact that the re-entrant jet flow is not the only observed closure mechanism. Indeed, for $\sigma = 1.15$ a side-entrant jet, hardly observable experimentally, is found to be responsible for the partial cut of the void fraction. Its development was found to be symmetrical. A key finding, which was firstly detected in a 3D simulation, is the influence of the shock waves due to collapses of the vapor structures. They play the role of sudden "break" for the spatial development of the vapor clouds. As a result, the cavity dynamics is governed by three different phenomena, which are the re-entrant jet, the side-entrant jet and the condensation shock waves. Consequently the symmetry between the two side cavities can be broken due to a scale effect resulting in a side-entrant jet. All of these phenomena have been experimentally observed on image sequences, and have been identified with a wavelet technique. Their frequencies of occurrence as well as their temporal positions are revealed.

The snapshot Proper Orthogonal Decomposition technique has been used on numerical and experimental data as a complementary tool for the study of the cavitation "transitory" regime at $\sigma = 1.15$. The three different section cuts show very similar results in terms of energy contributions, but differ in their spatial modal distribution.The number of cycles in experimental case is higher than in simulations, which leads to more significant results. The decomposition into 10 modes and the presentation of the first four is found to be sufficient for the good representation of the flow behavior. The values of the energy contribution for all of the modes 1 are superior to 1%, which implies the presence of cloud cavitation regime. The POD analysis reveals a clear horizontal symmetry of the multiphase flow for the experimental case and the superposed numerical one.

ACKNOWLEDGEMENT

The authors would like to acknowledge the financial support for the PhD thesis granted by SNECMA, part of SAFRAN group.

Appendix A: Development speed of sound in liquid

The constant entropy is given in Eq.A1 which after rewriting in terms of pressure and

$$c^2 = \left(\frac{\partial p}{\partial \rho}\right)_s \tag{A1}$$

temperature using Maxwell's relations, gives:

$$c^2 = \frac{\rho \left(\frac{\partial h}{\partial T}\right)_p}{\left(\frac{\partial \rho}{\partial p}\right)_T \left(\frac{\partial h}{\partial T}\right)_p + \left(\frac{\partial \rho}{\partial T}\right)_p \left[1 - \rho \left(\frac{\partial h}{\partial p}\right)_T\right]} \tag{A2}$$

Moreover, the use of Maxwell's relation Eq.A2 enables us to write down:

$$\frac{\partial c_v(T,v)}{\partial v} = T\frac{\partial^2 p}{\partial T^2} \tag{A3}$$

One can also write the internal energy in terms of the pressure and volume at constants volume and temperature, respectively as follows:

$$\left(\frac{\partial e}{\partial T}\right)_v = c_v(v,T) \tag{A4}$$

$$\left(\frac{\partial e}{\partial v}\right)_T = -t + T\left(\frac{\partial p}{\partial T}\right)_v \tag{A5}$$

If we use the hypothesis that the density of the liquid is constant, i.e. the liquid is incompressible, as well as $c_v(\rho_0, T)$ to be constant, one can write the formulation for the speed of sound in the liquid phase:

$$c_l^2 = \frac{N(p - p_{sat}(T) + K_0)}{\rho} + \frac{p}{\rho^2 C_{vl}}\left(\frac{\partial p_{sat}(T)}{\partial T} - \frac{N(p - p_{sat}(T) + K_0)}{\rho_{l,sat}(T)}\frac{\partial \rho_{sat}(T)}{\partial T}\right) \tag{A6}$$

Appendix B: Phase transition algorithm

Algorithm 1: Phase transition algorithm

Data: $\rho^n, (\rho u)^n, (\rho v)^n, (\rho w)^n, (\rho E)^n, T^n$: computed at previous time step
Result: $\rho^{n+1}, (\rho u)^{n+1}, (\rho v)^{n+1}, (\rho w)^{n+1}, (\rho E)^{n+1}$: given by solving Navier-Stokes equations
Compute: $e^{n+1} = E^{n+1} - \frac{1}{2}((u^{n+1})^2 + (v^{n+1})^2 + (w^{n+1})^2)$;
Initialize: $T^{n+1} = T^n$;
repeat
  (Re)-initialize: $T^* = T^{n+1}$;
  Compute: $\rho_{l,sat}(T^*)$ and $\rho_{v,sat}(T^*)$;
  if $\rho^{n+1} > \rho_{l,sat}(T^*)$ **then**
    $\alpha = 0$; /* liquid */
    $T^{n+1} = e^{n+1} - e_{l0}C_{vl} + T_0$
  end
  if $\rho^{n+1} < \rho_{v,sat}(T^*)$ **then**
    $\alpha = 1$; /* vapor */
    $T^{n+1} = e^{n+1} - e_{l0} - L_v(T_0)C_{vv} + T_0$
  end
  if $\rho_{v,sat}(T^*) \leq \rho^{n+1} \leq \rho_{l,sat}(T^*)$ **then**
    $\alpha = \rho^{n+1} - \rho_{l,sat}(T^*)\rho_{v,sat}(T^*) - \rho_{l,sat}(T^*)$; /* mixture */
    Solve: $T^{n+1} =$
    $\rho^{n+1}e^{n+1} - \alpha\rho_{v,sat}(T^{n+1})L_v(T_0) - \rho^{n+1}e_{l0}\alpha\rho_{v,sat}(T^{n+1})C_{vv} + (1-\alpha)\rho_{l,sat}(T^{n+1})C_{vl} + T_0$
  end
until $|T^{n+1} - T^*| \leq \epsilon$;
/* Computation of other parameters */;
if $\alpha = 0$ **then**
  $p^{n+1} = K_0\left[\left(\rho^{n+1}\rho_{l,sat}(T^{n+1})\right)^N - 1\right] + P_{sat}(T^{n+1})$;
  $\mu^{n+1} = \mu_{ref}10^{T_{ref}T^{n+1}-S0}$;
  $(c^{n+1})^2 = N\bar{P}\rho^{n+1} + p^{n+1}(\rho^{n+1})^2C_{vl}\left(P_{sat}(T^{n+1})T - N\bar{P}\rho_{l,sat}(T^{n+1})\rho_{l,sat}(T^{n+1})T\right)$;
  where $\bar{P} = p^{n+1} - P_{sat}(T^{n+1}) + K_0$;
end
if $\alpha = 1$ **then**
  $p^{n+1} = (\gamma - 1)\rho^{n+1}e^{n+1}$;
  $\mu^{n+1} = \mu_{ref}T^{n+1} + S_0T_{ref} + S_0\left(T^{n+1}T_{ref}\right)^{1.5}$;
  $\lambda_v = a_1T + a_2T^2 + a_3T^3 + a_4T^4$;
  $(c^{n+1})^2 = \gamma p^{n+1}\rho^{n+1}$;
end
if $0 < \alpha < 1$ **then**
  $p^{n+1} = P_{sat}(T^{n+1})$;
  $\frac{1}{\mu^{n+1}} = \frac{1-\xi}{\mu_l^{n+1}} + \frac{\xi}{\mu_v^{n+1}}$;
  $\lambda_v = a_1T + a_2T^2 + a_3T^3 + a_4T^4$;
  where,
  $\mu_l^{n+1} = \mu_{l,ref}10^{T_{l,ref}T^{n+1}-S_{l,0}}$;
  $\mu_v^{n+1} = \mu_{v,ref}T^{n+1} + S_{v,0}T_{v,ref} + S_{v,0}\left(T^{n+1}T_{v,ref}\right)^{1.5}$;
  $(c^{n+1})^2 = \rho^{n+1}\left(\alpha\rho_{v,sat}(c_v^{n+1})^2 + 1 - \alpha\rho_{l,sat}(c_l^{n+1})^2\right)^{-1}$;
  where,
  $(c_l^{n+1})^2 = N\bar{P}\rho^{n+1} + p^{n+1}(\rho^{n+1})^2C_{vl}\left(P_{sat}(T^{n+1})T - N\bar{P}\rho_{l,sat}(T^{n+1})\rho_{l,sat}(T^{n+1})T\right)$;
  $(c_v^{n+1})^2 = \gamma p^{n+1}\rho^{n+1}$;
end
Compute: $H^{n+1} = E^{n+1} + \frac{p^{n+1}}{\rho^{n+1}}$

REFERENCES

[1]R. Fortes-Patella and J.-L. Reboud. A new approach to evaluate the cavitation erosion power. *J. Fluids Eng.*, 120:335–344, 1998.

[2]Y. Tsujimoto, K. Kamijo, and C. E. Brennen. Unified treatment of flow instabilities of turbomachines. *Int. J. Prop. and Power*, 17:636–643, 2001.

[3]B. Pouffary, R. Fortes-Patella, J.-L. Reboud, and P.-A. Lambert. Numerical simulation of 3d cavitating flows: Analysis of cavitation head drop in turbomachinery. *J. Fluids Eng.*, 130:061301, 2008.

[4]I. Mejri, F. Bakir, R. Rey, and T. Belamri. Comparison of computational results obtained from a homogeneous cavitation model with experimental investigations of three inducers. *J. Fluids Eng.*, 128:1308–1323, 2006.

[5]A. Danlos, J. E. Méhal, F. Ravelet, O. Coutier-Delgosha, and F. Bakir. Study of the cavitating instability on a grooved venturi profile. *Int. J. Heat and Fluid Flow*, 136:101302, 2014.

[6]P. Brandner, G. J. Walker, P. N. Niekamp, and B. Anderson. An experimental investigation of cloud cavitation about a sphere. *J. Fluid Mech.*, 656:147–176, 2010.

[7]M. Wosnik and R. E. A. Arndt. Measurements in high void-fraction bubbly wakes created by ventilated supercavitation. *J. Fluids Eng.*, 135:011304, 2013.

[8]S. L. Ceccio. Friction drag reduction of external flows with bubble and gas injection. *Ann. Rev. Fluid Mech.*, 42:183–203, 2010.

[9]Q. Le, J.P. Franc, and J.M. Michel. Partial cavities: Global behavior and mean pressure distribution. *J. Fluids Eng.*, 115:243–248, 1993.

[10]T.M. Pham, F. Larrarte, and D.H. Fruman. Investigation of unsteady sheet cavitation and cloud cavitation mechanisms. *J. Fluids Eng.*, 121:289–296, 1999.

[11]M. Callenaere, J. P. Franc, J.M. Michel, and M. Riondet. The cavitation instability induced by the development of a re-entrant jet. *J. Fluid Mech.*, 444:223–256, 2001.

[12]B. Stutz and J.-L. Reboud. Measurements within unsteady cavitation. *Exp. In Fluids*, 29:545–552, 2000.

[13]M. Dular, I. Khlifa, S. Fuzier, M. Adama Maiga, and O. Coutier-Delgosha. Scale effect on unsteady cloud cavitation. *Exp. In Fluids*, 53:1233–1250, 2012.

[14]H. Ganesh, S. A. Makiharju, and S. L. Ceccio. Partial cavity shedding due to the propagation of shock waves in bubbly flows. *Proceedings of the 30^{th} symposium on naval hydrodynamics*, 2014.

[15]J. Decaix and E. Goncalvès. Investigation of three-dimensional effects on a cavitating venturi flow. *Int. J. Heat and Fluid Flow*, 44:576–595, 2013.

[16]G. Chen, G. Wang, C. Hu, B. Huang, Y. Gao, and M. Zhang. Combined experimental and computational investigation of cavitation evolution and excited pressure fluctuation in a convergent-divergent channel. *Int. J. Multiphase Flow*, 72:133–140, 2015.

[17]N. Dittakavi, A. Chunekar, and S. Frankel. Large eddy simulation of turbulent-cavitation interactions in a venturi nozzle. *J. Fluids Eng.*, 132:121301, 2010.

[18]B. Charrière, J. Decaix, and E. Goncalvès. A comparative study of cavitation models in a venturi flow. *Eur. J. Mech. B/Fluids*, 49:287–297, 2015.

[19]P. Tomov, S. Khelladi, F. Ravelet, C. Sarraf, F. Bakir, and P. Vertenoeuil. Experimental study of aerated cavitation in a horizontal venturi nozzle. *Exp. Thermal and Fluid Science*, 70:85–95, 2016.

[20]G. H. Schnerr, I. H. Sezal, and S. J. Schmidt. Numerical investigation of three-dimensional cloud cavitation with special emphasis on collapse induced shock dynamics. *Phys. Fluids*, 20, 2008.

[21]M. Dular and R. Bachert. The issue of strouhal number definition in cavitating flow. *J. of Mech. Eng.*, 55:666–674, 2009.

[22]R. Saurel, J. P. Cocchi, and P. B. Butler. Numerical study of cavitation in the wake of a hypervelocity underwater projectile. *Int. J. Prop. and Power*, 15:513–522, 1999.

[23]O. Le Métayer, J. Massoni, and R. Saurel. Elaboration des lois d'etat d'un liquide et de sa vapeur pour les modèles d'ecoulements diphasiques. *Int. J. Thermal Science.*, 43:265–276, 2004.

[24]E. Schmidt. *Properties of Water and Steam in SI-Units; 0-800° C, 0-1000 bar.* Springer-Verlag, 1989.

[25]H. Vogel. *Phys. Z.*, 22:645, 1921.

[26]G.S. Fulcher. *J. Am. Ceram. Soc.*, 8:339, 1925.

[27]G.S. Fulcher and W. Hesse. *Z. Anorg. Allg. Chem.*, 156:245, 1926.

[28]W. Sutherland. The viscosity of gases and molecular force. *Philosophical Magazine Series 5*, 36:507–531, 1893.

[29]I. Dincer, C.O. Colpan, O. Kizilkan, and M.A. Ezan. *Progress in Clean Energy, Volume 2. Novel Systems and Applications.* Springer-Verlag, 2015.

[30]A. Wood. *A text book of sound.* G. Bell and Sons Ltd. London, 1960.

[31]R. Saurel, P. Boivin, and O. Le Metayer. A general formulation for cavitating , boiling and evaporating flows. *Computers & Fluids*, 128:53–64, 2016.

[32]S. Khelladi, X. Nogueira, F. Bakir, and I. Colominas. Toward a higher order unsteady finite volume solver based on reproducing kernel methods. *Comp. Meth. in App. Mech. and Eng.*, 200:2348–2362, 2011.

[33]X. Nogueira, I. Colominas, L. Cueto-Felgueroso, and S. Khelladi. On the simulation of wave propagation with a higher-order finite volume scheme based on reproducing kernel methods. *Comp. Meth. in App. Mech. and Eng.*, 199:1471–1490, 2010.

[34]X. Nogueira, S. Khelladi, L. Cueto-Felgueroso, F. Bakir, I. Colominas, and H. Gómez. Implicit large-eddy simulation with a moving least squares-based finite volume method. *IOP Conference Series: Materials Science and Engineering*, 10:012235, 2010.

[35]E. Turkel. Review of preconditioning methods for fluid dynamics. *Applied Numerical Mathematics*, 12:257–

284, 1993.

[36]X. Nogueira, L. Ramirez, S. Khelladi, J.-C. Chassaing, and I. Colominas. A high-order density-based finite volume method for the computation of all-speed flows. *Comp. Meth. in App. Mech. and Eng.*, 298:229–251, 2016.

[37]E. Shima and K. Kitamura. On new simple low-dissipation scheme of ausm-family for all speeds. *AIAA paper*, 49:1–15, 2009.

[38]K. Kitamura, M.-S. Liou, and C.-h. Chang. Extension and comparative study of ausm-family schemes for compressible multiphase flow simulations. *Commun. Comput. Phys.*, 1:632–674, 2006.

[39]S. Hickel. *Implicit Turbulence Modeling for Large-Eddy Simulation.* PhD thesis, Technische Universitat Munchen, 2008.

[40]X. Nogueira, L. Cueto-Felgueroso, I. Colominas, and H. Gómez. Implicit large eddy simulation of non-wall-bounded turbulent flows based on the multiscale properties of a high-order finite volume method. *Comp. Meth. in App. Mech. and Eng.*, 199:615–624, 2010.

[41]P. Holmes, G. Berkooz, and J. Lumley. *Turbulence, Coherent Structures, Dynamical Systems and Symmetry.* Cambridge University Press, 2013.

[42]A. Danlos, F. Ravelet, O. Coutier-Delgosha, and F. Bakir. Cavitation regime detection through proper orthogonal decomposition: Dynamics analysis of the sheet cavity on a grooved convergentdivergent nozzle. *Int. J. Heat and Fluid Flow*, 47:9–20, 2014.

[43]B. Patte-Rouland, A. Danlos, G. Lalizel, E. Rouland, and P. Paranthoen. Proper orthogonal decomposition used for determination of the convection velocity of the initial zone of the annular jet. aerodynamic study and control of instabilities. *J. of Fluid Dynamics*, 1:1–10, 2012.

[44]E. A. Christensen, M. Brons, and J. N. Sorensen. Evaluation of pod-based decomposition techniques applied to parameter-dependent non-turbulent flows. *SIAM Journal of Scientific Computing*, 21:1419–1434, 2000.

[45]T. Brenner. Practical aspects of the implementation of reduced-order models based on proper orthogonal decomposition. *PhD Thesis, University of Texas Austin*, 2011.

[46]L. Sirovich. Turbulence and the dynamics of coherent structures part one: coherent structures. *Quarterly of Applied Mathematics*, XLV:561–571, 1987.

[47]M. Kjeldsen and R. E. A. Arndt. Joint time frequency analysis techniques : a study of transitional dynamics in sheet/cloud cavitation. In *Symposium on Cavitation*, 2001.

[48]P. Brandner, B. W. Pierce, and K. L. de Graaf. Cavitation about a jet in crossflow. *J. Fluid Mech.*, 768:141–174, 2015.

[49]C. Torrence and G. P. Compo. A practical guide to wavelet analysis. *Bull. Amer. Meteor. Soc*, 79, 1999.

[50]H. Ganesh. *Bubbly shock propagation as a cause of sheet to cloud transition of partial cavitation and stationary cavitation bubbles forming on a delta wing vortex.* PhD thesis, University of Michigan, 2015.

[51]P. Tomov, A. Danlos, S. Khelladi, F. Ravelet, Sarraf C., and F. Bakir. Pod study of aerated cavitation in a venturi nozzle. *Journal of Physics: Conference Series*, 656:012171, 2015.

[52]R. B. Wade and A. J. Acosta. Experimental Observations on the Flow Past a Plano-Convex Hydrofoil. *J. Basic Eng.*, 88:273–282, 1966.

[53]E.-J. Foeth, T. van Terwisga, and C. van Doorne. On the collapse structure of an attached cavity on a three-dimensional hydrofoil. *J. Fluids Eng.*, 130:071303, 2008.

[54]H. Ganesh, S. A. Mäkiharju, and S. L. Ceccio. Interaction of a compressible bubbly flow with an obstacle placed within a shedding partial cavity. *Journal of Physics: Conference Series*, 656:012151, 2015.

[55]C. E. Brennen. Fundamentals of multiphase flow. *Cambridge University Press*, 2005.

[56]M. S. Mihatsch, S. J. Schmidt, and N. A. Adams. Cavitation erosion prediction based on analysis of flow dynamics and impact load spectra. *Phys. Fluids*, 27:103302, 2015.